Applied Catalysis B: Environmental 196 (2016) 155–173

Contents lists available at ScienceDirect

Applied Catalysis B: Environmental

journal homepage: www.elsevier.com/locate/apcatb

Natural magnesium oxide (MgO) catalysts: A cost-effective sustainable alternative to acid zeolites for the *in situ* upgrading of biomass fast pyrolysis oil

S.D. Stefanidis[a,b], S.A. Karakoulia[a], K.G. Kalogiannis[a], E.F Iliopoulou[a], A. Delimitis[a], H. Yiannoulakis[c], T. Zampetakis[c], A.A. Lappas[a,*], K.S. Triantafyllidis[d,*]

[a] *Chemical Process and Energy Resources Institute, CERTH, P.O. Box 60361, Thermi, 570 01 Thessaloniki, Greece*
[b] *Department of Mechanical Engineering, University of Western Macedonia, Kozani, 50100 Greece*
[c] *Grecian Magnesite S.A., Research Center, Vasilika, 570 06, Thessaloniki, Greece*
[d] *Department of Chemistry, Aristotle University of Thessaloniki, 541 24 Thessaloniki, Greece*

ARTICLE INFO

Article history:
Received 16 March 2016
Received in revised form 11 May 2016
Accepted 16 May 2016
Available online 17 May 2016

Keywords:
Catalytic fast pyrolysis
Biomass
Bio-oil upgrading
Aromatization
Ketonization
Condensation
Acid catalysts
Zeolites
Base catalysts
Magnesia

ABSTRACT

The thermal and catalytic fast pyrolysis of biomass aims at the production of pyrolysis oil (bio-oil), which can be utilized as a source of chemicals or as a bio-crude for the production of hydrocarbon fuels. We investigated low-cost, naturally derived basic MgO materials as catalysts for the catalytic fast pyrolysis of lignocellulosic biomass as alternatives to classical acidic zeolite catalysts. The MgO catalysts were produced from natural magnesite mineral without any significant treatment besides calcination, crushing and sieving. Their structure, composition, porosity, morphology and surface properties were thoroughly examined by XRD, XRF, N_2 porosimetry, SEM, TEM, TPD-CO_2 and TPD-NH_3. The physicochemical characteristics of the MgO catalysts depended mainly on the different production conditions (duration and temperature of calcination). Despite their negligible acidity, the MgO catalysts effectively reduced the oxygen content of the produced bio-oil and exhibited similar or even better performance compared to that of an industrial ZSM-5 catalyst formulation (*i.e. non-catalytic pyrolysis:* 38.9 wt.% organic bio-oil with 38.7 wt.% O_2; *ZSM-5 based catalyst:* 20.7 wt.% organic bio-oil with 30.9 wt.% O_2; *selected natural MgO catalysts:* 25.7 wt.% organic bio-oil with 31.0 wt.% O_2 or 21.1 wt.% organic bio-oil with 28.4 wt.% O_2). The basic sites of the MgO catalysts favored reduction of acids and deoxygenation *via* ketonization and aldol condensation reactions, as indicated by the product distribution and the composition of the bio-oil. Oxygen was removed mainly *via* the preferred pathway of CO_2 formation, compared to CO and water as in the case of ZSM-5 zeolite. On the other hand, reaction coke slightly increased over the MgO catalysts as compared to ZSM-5; however, the MgO formed coke was oxidized/burnt at significantly lower temperatures compared to that of ZSM-5, thus enabling MgO regeneration by relatively mild calcination in air. A systematic correlation of product yields and oxygen content of bio-oil with the physicochemical properties of the MgO catalysts has been established.

© 2016 Elsevier B.V. All rights reserved.

1. Introduction

The increase in world energy demand, environmental concerns and the shortage of fossil fuels have driven interest in alternative energy sources. Lignocellulosic biomass is such an alternative and renewable energy source that is abundant, cheap and can be directly converted into liquid, solid and gaseous fuels [1]. A sustainable, cost effective utilization of lignocellulosic biomass can diversify the energy balance and reduce the dependence on fossil fuels, leading to a more secure energy supply. Biomass has the added benefit of being compatible with current energy production technologies while it can be also converted to a wide range of commodity chemicals [2–4]. Furthermore, valorization of agricultural wastes, energy crops and forestry by-products, especially *via* decentralized small-size processing units, can offer additional support to the local rural economy.

Lignocellulosic biomass can be converted into liquid, solid and gaseous products *via* the fast pyrolysis process [5–8]. The liquid product (pyrolysis oil or bio-oil) yield can reach up to

* Corresponding authors.
E-mail addresses: angel@cperi.certh.gr (A.A. Lappas), ktrianta@chem.auth.gr, ktrianta@cperi.certh.gr (K.S. Triantafyllidis).

http://dx.doi.org/10.1016/j.apcatb.2016.05.031
0926-3373/© 2016 Elsevier B.V. All rights reserved.

75 wt.% on biomass, depending on the process conditions and the biomass feedstock. The bio-oil is a complex mixture of oxygenated compounds (*i.e.* ketones, phenolics, furans, acids, aldehydes, etc.) derived from the thermal degradation of the holocellulose and lignin fractions in the biomass [9]. Due to its composition, the bio-oil exhibits low calorific value, high viscosity, corrosivity to common metals, immiscibility with hydrocarbon fuels and instability under storage and transportation conditions [9]. It is therefore a low quality product that needs to be upgraded before it can be introduced into the market.

One approach for the production of an upgraded bio-oil is the catalytic fast pyrolysis of biomass, which takes place under the same conditions as thermal fast pyrolysis, with the difference being that pyrolysis vapors come in contact with a solid catalyst prior to their condensation. The catalytic reactions that take place on the catalyst's surface enhance the removal of oxygen in the form of CO_2, CO and H_2O, thus leading to the formation of a bio-oil with tailored composition and improved properties. Furthermore, a de-oxygenated bio-oil can serve as bio-crude and can be treated down-stream, in admixtures with petroleum fractions (*i.e.* gas-oil) in classical (hydro)cracking refinery processes for the production of gasoline and diesel [10]. A wide variety of materials has been suggested as candidate catalysts for the process. Mainly acid catalysts have been studied, such as microporous zeolites, mesoporous aluminosilicates and metal-modified zeolites, while basic catalysts have also been scarcely considered [11]. Naturally-derived activated serpentine and olivine catalysts have been recently investigated for the production of bio-oil with reduced oxygen content [12].

Acid catalysts favor dehydration, decarbonylation, cracking and aromatization reactions [11,13–20]. Aromatization reactions that are favored by the presence of strong zeolitic acid sites lead to the formation of highly valuable monocyclic aromatic hydrocarbons, BTX (*i.e.* benzene, toluene, xylene). However, aromatization reactions are hard to control and contribute also to the formation of polycyclic aromatic hydrocarbons (PAH), which are undesirable due to their known carcinogenic and mutagenic potential. Additionally, PAH can act as precursors of catalytic coke, leading to catalyst deactivation and loss of biomass carbon towards solid products rather than its transformation into desirable liquid products [21]. Among the various acid catalysts, ZSM-5 zeolite is the most frequently studied, as it increases the yield of monocyclic aromatic hydrocarbons and suppresses coke formation due to its unique micropore structure and relatively strong Brönsted acidity [22].

In a previous study [14], we carried out screening of various acidic and basic catalysts for the *in situ* catalytic upgrading of biomass pyrolysis vapors in a fixed bed reactor. The results indicated different bio-oil deoxygenation pathways between the basic and acidic materials. Specifically, the basic catalysts induced high CO_2 yields and bio-oil with decreased acid concentration and high content of ketones, mainly cyclopentanones and cyclopentenones. Ketonization of acids, with simultaneous formation of CO_2, and aldol condensation of aldehydes and smaller ketones were suggested as the prevalent reactions taking place [23,24]. On the other hand, the use of acid zeolitic catalysts (*i.e.* ZSM-5) led to aromatic bio-oils, as mentioned above, with reduced content of oxygenated compounds, while CO and H_2O were the dominant by-products. In terms of carbon efficiency, it would be more desirable to remove oxygen from biomass *via* CO_2 (two O atoms for one C atom) than *via* CO or H_2O. Thus, the use of basic catalysts may open new paths in biomass fast pyrolysis, with regard to the carbon efficiency of the process, the composition of the produced bio-oil and its down-stream upgrading. To this end, one of the most attractive candidates as basic catalyst for biomass pyrolysis would be magnesium oxide (MgO). Going further in line with the green chemistry principles, the use of natural MgO, *i.e.* derived by the calcination of mineral magnesite, could offer a promising cost-effective alternative to the classical synthetic industrial zeolites and related acid catalysts. Catalyst cost is one of the most crucial parameters of catalytic biomass pyrolysis with regard to the economics of the process [25]. The expected tolerance of basic oxide catalysts to deactivation induced by the biomass alkali metals and related ash (*i.e.* Na, K, Ca, Si, etc.) in contrast to the acidic zeolites, is an additional benefit in terms of profitability and economics.

Natural magnesium oxide is produced industrially by thermal decomposition of magnesium carbonate mineral ($MgCO_3$ or magnesite). Natural magnesia can be categorized into two main types, namely caustic-calcined magnesia (CCM, *i.e.* chemically reactive porous magnesium oxide with small crystal size) and dead-burnt magnesia (DBM, *i.e.* non-porous magnesium oxide with high crystal size and very low reactivity), depending on the severity of the thermal treatment of the raw material. Careful beneficiation (process in the mining industry for removing undesirable mineral mixtures form an ore to produce a higher grade product) and calcination of magnesite, leads to CCMs with tuned chemical composition and crystal/particle morphology, thus substantially increasing their added value and broadening their application range to include, among others, the production of catalysts and catalyst supports, a market otherwise typically served by synthetic CCM. Synthetic MgO is usually derived by calcination of $Mg(OH)_2$.

In this work, we investigated the *in situ* upgrading of biomass pyrolysis vapors over various naturally derived basic MgO catalysts. The upgrading potential of these catalysts was compared to that of an industrial ZSM-5 based catalyst formulation, as well as to synthetic MgO materials. Differences in reaction mechanisms and bio-oil composition induced by the basic MgO catalysts compared to acid zeolites were thoroughly discussed.

2. Experimental

2.1. Materials and catalyst preparation

In total, 17 MgO catalysts were investigated (Table 1). These included one natural olivine and 14 natural MgO catalysts prepared either industrially (beneficiation and rotary kiln calcination) or in the laboratory from the calcination of two raw magnesite samples of different purity, *i.e.* Raw-1 (high purity) and Raw-2 (low purity). Depending on the content of impurities (mainly SiO_2 and CaO), the various calcined MgOs listed in Table 1, were characterized as of high purity (SiO_2 and CaO up to 2 wt.%), medium purity (SiO_2 2–7 wt.% and CaO up to 2.5 wt.%), and low purity (SiO_2 25–31 wt.% and CaO 2.9-3.8 wt.%). All natural MgO and olivine samples originated from Grecian Magnesite's Yerakini mine in Northern Greece. In addition, two synthetic industrial caustic calcined magnesia samples were also studied. More information about the various MgO samples are given below.

2.1.1. Laboratory caustic calcined magnesia (CCM) samples

For the laboratory CCM samples (LabCCM-1 to LabCCM-7), the two raw magnesite samples (Raw-1 and Raw-2) were crushed in a laboratory jaw crusher to ±5 mm. An amount of 350 g was then placed on a ceramic plate and calcined in a 1.5 kW laboratory furnace at various temperatures (700–1150 °C) and residence times (60–240 min) to produce MgO samples of varying crystal size, chemical composition and specific surface area (Tables 1 and 2). Ramp-up times to the desired temperature were between 1–3 h, depending on the desired end temperature. After calcination, the samples were milled to ±200 μm in a laboratory disk mill and the 90–200 μm fraction was separated with vibrating sieves.

Table 1
Physicochemical properties of MgO and olivine catalysts.

Catalyst	Granulometry (μm)	Calcination		Chemical composition (XRF)							Crystal size (nm)[b]
		Temp. (°C)	Time (min)	MgO[a] (%)	SiO_2 (%)	CaO (%)	Fe_2O_3 (%)	Al_2O_3 (%)	SO_3 (%)	LOI (1000 °C)	
Raw-1	90–180	–	–	46.69	1.72	0.80	0.09	0.01	0.03	50.66	–
Raw-2	90–180	–	–	44.06	6.97	1.79	0.47	0.08	0.08	46.55	–
IndCCM-1	90–180	Industrial kiln profiles		92.62	1.21	1.06	0.02	0.09	0.16	4.84	19.5 (19.9)
IndCCM-2	90–180	with max temperatures		86.65	5.93	2.44	0.13	0.10	0.22	4.53	24.1 (23.2)
IndCCM-3	90–180	800–1200 °C		93.25	1.98	2.11	0.08	0.01	0.21	2.36	28.5 (29.4)
IndCCM-4	90–180			90.44	5.30	2.31	0.15	0.11	0.13	1.56	42.9 (43.3)
IndCCM-5	90–200			92.26	4.22	1.96	0.05	0.10	0.09	1.32	30.5
LabCCM-1	90–200	800	240	92.95	2.16	2.17	0.14	0.11	0.03	2.44	21.2
LabCCM-2	90–200	1150	150	94.00	2.21	2.22	0.16	0.07	0.04	1.30	31.6
LabCCM-3	90–200	700	60	87.77	5.14	2.20	0.18	0.08	0.02	4.62	12.1 (12.0)
LabCCM-4	90–200	700	60	62.41	27.10	3.83	0.76	0.42	0.11	5.37	13.0
LabCCM-5	90–200	800	240	61.89	31.38	3.71	0.78	0.52	0.12	1.60	20.1
LabCCM-6	90–200	1100	45	69.89	25.20	2.90	0.78	0.51	0.14	0.58	33.2
LabCCM-7	90–200	800	60	87.02	6.67	2.48	0.24	0.05	0.02	3.53	18.6
SynCCM-1	90–200	Industrial kiln profile with max temperature 1200 °C		95.3	0.21	1.32	0.10	0.12	1.03	2.02	70.4 (69.8)
SynCCM-2	90–200	Industrial kiln profile with max temperature 500 °C		89.4	0.31	0.82	0.12	0.10	1.02	8.24	15.3 (8.3)
DBM-1	90–180	Industrial kiln profiles		89.56	5.78	1.63	0.62	0.11	0	2.30	79.8
DBM-2	90–180	with max		95.05	2.79	1.83	0.12	0.10	0	0.11	–
Olivine	90–200	temperature >1800 °C	–	46.47	42.93	0.56	8.50	–	–	1.45	–

[a] Nominal percentage calculated by the abstraction of the sum of impurities (expressed as wt.% of oxides) and of LOI (wt.%, humidity, hydroxides and residual carbonates) from 100.
[b] From Scherrer equation using XRD data of peak 2θ = 42.9°; the values correspond to the crystal size of the catalysts after being re-calcined at 500 °C for 3 h, while the values in parentheses refer to the crystal size of the as-produced materials prior to the final re-calcination.

2.1.2. Industrial caustic calcined magnesia (CCM) and dead-burnt magnesia (DBM) samples

The industrial CCM samples (IndCCM-1 to IndCCM-5) were produced by the calcination of raw magnesite in rotary kilns. Controlled temperature and residence time conditions were applied, depending on the desired crystal size and specific surface area. Maximum temperatures varied between 800 and 1200 °C. Representative samples of the Run-of-Kiln material (0–14 mm) were selected, crushed to ±5 mm and milled at ±180 μm in the laboratory. The 90–180 μm fraction was separated out of the samples with the use of vibrating sieves. The industrial dead-burnt MgO samples (DBM-1 and DBM-2) were produced in an analogous manner, the only difference being the higher kiln temperatures (higher than 1800 °C in a developed sintering zone in the kiln).

2.1.3. Olivine and synthetic caustic calcined magnesia samples

One olivine sample was produced from dunite rock, crushed to ±5 mm and milled to ±200 μm with a disk mill. The 90–200 μm fraction was separated with vibrating sieves. Finally, the two synthetic MgO samples (SynCCM-1 and SynCCM-2) were commercially available. These were industrial grades, produced by $Mg(OH)_2$ that was precipitated from sea-water with the use of calcined dolomite (MgO·CaO). The $Mg(OH)_2$ was calcined in an industrial rotary kiln with tuned temperature profiles (T_{max} of 500 and 1200 °C).

2.1.4. Other materials

In addition to the catalytic tests with MgO catalysts, thermal pyrolysis with inert silica sand and catalytic pyrolysis tests with an acidic ZSM-5 based zeolitic catalyst were also performed for comparison purposes. The ZSM-5 catalyst was an industrial ZSM-5 based formulation that consisted of about 30% crystalline zeolite diluted in a silica-alumina matrix (138 m^2/g surface area, 0.037 cm^3/g and 0.071 cm^3/g micro- and meso/macropore volume respectively).

2.2. Characterization of MgO and olivine catalysts

All characterization techniques took place on re-calcined MgO samples, unless stated differently. Re-calcination occurred at 500 °C for 3 h in air in order to stabilize the materials prior to their use as catalysts for the biomass pyrolysis experiments.

X-ray fluorescence (Spectro X-Lab 2000, pressed tablets of samples) was used for the chemical analysis of the samples (nominal composition of elements expressed as oxides). Loss on ignition (LOI) was determined by igniting 2 g samples in a 1.5 kW laboratory furnace for 1 h at 1000 °C.

Powder X-ray diffraction (XRD) was applied to identify the crystal structure of the materials using a Siemens Diffraktometer D5000 equipped with Cu Kα X-ray radiation and a curved crystal graphite monochromator operating at 45 kV and 100 mA; counts were accumulated in the range of 5–75° 2θ every 0.02° (2θ) with counting time 2 s per step. The crystal size (L) was also determined by measuring the width at half maximum, $\beta_{1/2}$, of the MgO's main peak at 2θ = 42.9° as an input to the Scherrer equation ($L\,[nm] = K\,\lambda/\beta_{1/2}\cos\theta$).

N_2 adsorption-desorption experiments at −196 °C were performed on an Automatic Volumetric Sorption Analyzer (Autosorb-1, Quantachrome) for the determination of surface area (BET method), total pore volume at P/Po = 0.99, micropore volume (t-plot method), and pore size distribution (BJH method) of the samples that were previously outgassed at 150 °C for 16 h under 5×10^{-9} Torr vacuum.

Scanning Electron Microscopy (SEM) images were obtained on a JEOL 6300 microscope in order to study the morphology of selected samples while the texture and morphology at the nanoscale was

studied with High Resolution-Transmission Electron Microscopy (HR-TEM) images obtained on a JEOL 2011 HRTEM microscope.

The basic characteristics of the MgO catalysts were studied with CO_2-temperature programmed desorption (TPD-CO_2). In a typical experiment, 0.2 g of the sample were loaded in a fixed bed quartz reactor and pretreated at 600 °C in He for 1 h, followed by cooling to 80 °C under He flow and subsequent treatment with a flow of 40% CO_2/He for 1 h at 80 °C. Flushing with pure He at 80 °C for 3 h was then applied to remove the physisorbed CO_2. TPD analysis was carried out from 80 to 600 °C at a heating rate of 10 °C/min and a He flow rate of 50 ml/min. The composition of the exit gas was monitored online by a quadrupole mass analyzer (Omnistar, Balzer). Quantitative analysis of the desorbed CO_2 was based on the fragment $m/z = 44$.

The acidic characteristics of the MgO catalysts were studied with NH_3-temperature programmed desorption (TPD-NH_3). In a typical experiment, 0.1 g of the sample were loaded in a fixed bed quartz reactor and pretreated at 550 °C in He for 1 h, followed by cooling to 100 °C under He flow and subsequent treatment with a flow of 5% NH_3/He for 1 h at 100 °C. Flushing with pure He (30 ml/min) at 100 °C for 12 h was then applied to remove the physisorbed ammonia. The analysis was carried out from 100 to 800 °C at a heating rate of 10 °C/min and a He flow rate of 50 ml/min. The composition of the exit gas was monitored online by a quadrupole mass analyzer (Omnistar, Balzer). Quantitative analysis of the desorbed ammonia was based on the fragment $m/z = 15$.

Temperature programmed oxidation (TPO) of coked catalysts (after catalytic fast pyrolysis experiments) were performed in the same set-up used for the TPD experiments. In a typical run, 0.2 gr of the coked catalyst was initially dried at 100 °C under He flow, and was then subjected to programmed heating up to 800 °C, under a flow of 20% O_2 in He (50 cc/min) with a heating rate of 10 °C/min. The production of CO_2 ($m/z = 44$) was continuously monitored by the on-line GC–MS.

2.3. Catalytic pyrolysis tests

The catalytic biomass fast pyrolysis tests were performed on a bench-scale fixed bed tubular reactor (ID 1.4 cm, height 36 cm), made of stainless steel 316 and heated by a 3-zone furnace. The feedstock biomass was a commercial beech wood sawdust (Lignocel HBS 150-500 purchased from JRS), with the following elemental analysis: carbon: 45.98 wt.%, hydrogen: 6.39 wt.%, oxygen: 46.97 wt.%, ash: 0.66 wt.%. A specially designed piston system was used to introduce the solid biomass into the reactor. A detailed description of the experimental unit has been also previously reported [14]. The amount of biomass used in all experiments was 1.5 g and the amount of silica sand (in the non-catalytic, thermal pyrolysis experiments) or of catalyst (in the catalytic experiments) was 0.7 g. In a typical pyrolysis experiment, the solid biomass was inserted from the top of the reactor and was pushed down instantaneously with the aid of the piston in the hot reactor zone, where it was vaporized at 500 °C. The produced pyrolysis vapors were then driven downwards through the catalyst's bed with the aid of a constant N_2 flow (100 cm^3/min) for 15 min, while additional purging with N_2 (50 cm^3/min) was performed for another 10 min.

The pyrolysis product vapors were condensed in a pre-weighted glass receiver submerged in a cooling bath (−17 °C). The obtained bio-oil comprised of an aqueous phase, a liquid organic phase and viscous organic deposits on the receiver walls. Ethyl lactate was used to homogenize the bio-oil before being submitted to water content analysis (Karl-Fischer titration, ASTM E203-08) and elemental composition analysis (Leco CHN-800 elemental analyzer). The organic phase of bio-oil separated by the use of dichloromethane was analyzed by GC–MS (Agilent 7890A/5975C). The NIST05 mass spectral library was used for the identification of the compounds found in the bio-oil, while internal libraries and software were used for their categorization into main functional groups. The amount of the solid residue left in the reactor, which consisted mainly of charcoal and coke-on-catalyst formed by thermal and/or catalytic cracking, was determined by direct weighing. Non-condensable gases were measured by the liquid displacement method and were analyzed by GC equipped with TCD and FID (HP 5890 Series II). More details on analytic procedures are provided in Supporting information.

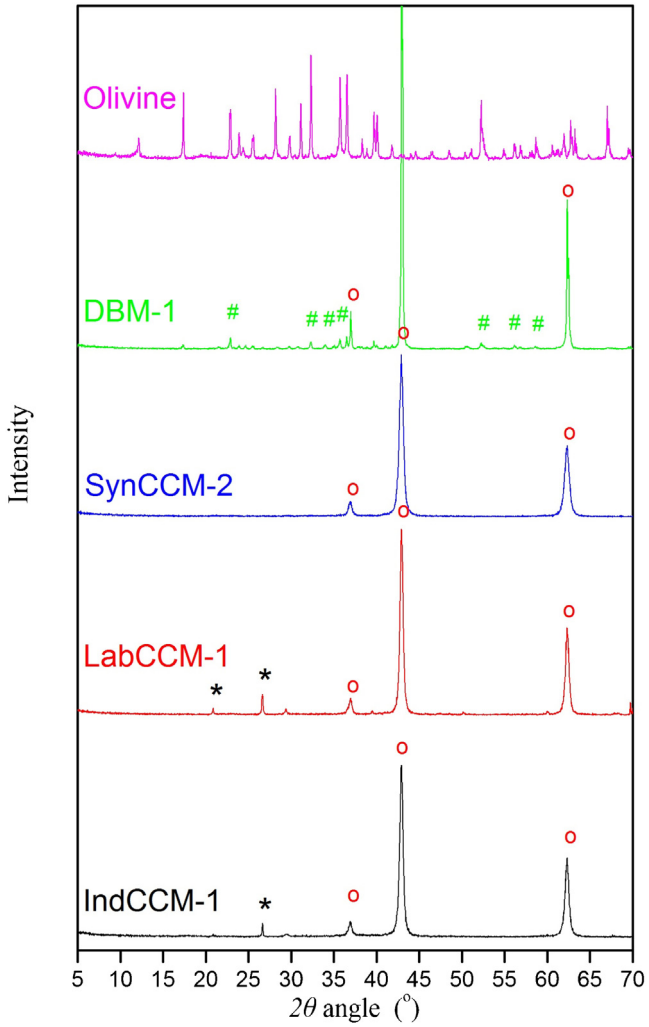

Fig. 1. XRD patterns of selected natural (industrial and laboratory calcined) and synthetic MgO materials. Symbols: (o) MgO, Periclase, Cubic; (*) SiO2, Quartz, Hexagonal; (#) Mg_2SiO_4, Forsterite, Orthorombic. Olivine: typical XRD pattern of olivine comprising of Forsterite – $2(Mg_{0.91}Fe_{0.09})O{\cdot}SiO_2$, Antigorite – $Mg_3Si_2O_5(OH)_4$, Enstatite – $Mg_2(Si_2O_6)$ and Talc – $Mg_3(OH)_2Si_4O_{10}$ phases.

3. Results and discussion

3.1. Catalyst characterization

3.1.1. Chemical composition

Table 1 summarizes the chemical composition of all MgO catalyst samples as determined by XRF and the corresponding loss on ignition (LOI). The magnesite samples Raw-1 and Raw-2 were of high and low purity, respectively, while the calcined MgO samples (CCM and DBM) varied in chemical purity, expressed as the percentage content of MgO, between 62–95%. Main impurities were silicon (as SiO_2, 0.2–31.4 wt.%), calcium (as CaO, 0.8–3.8 wt.%) and LOI (0.1–8.2 wt.%), the latter representing the carbonate and mois-

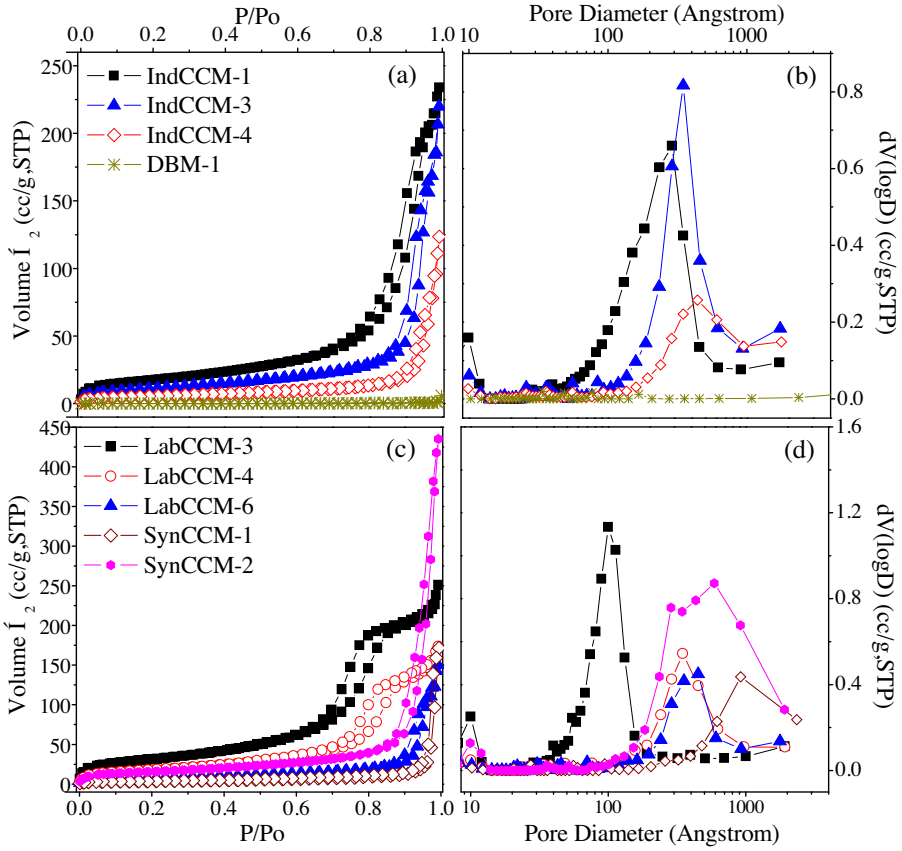

Fig. 2. (a, c) N_2 adsorption-desorption isotherms of selected natural MgOs (industrial and laboratory calcined) and synthetic MgOs, and (b, d) their respective pore size distribution curves (BJH method, adsorption data).

ture/hydroxides content of the samples (*i.e.* CO_2 and H_2O). The industrial MgO samples (IndCCM and DBM) were of high to medium purity, with IndCCM-1 having the lowest amount of SiO_2 and CaO impurities. Laboratory samples LabCCM-1 to LabCCM-3 and LabCCM-7 contained relatively low amount of impurities as they were produced *via* calcination of Raw-1, while samples LabCCM-4 to LabCCM-6, produced by the calcination of Raw-2, had very high contents of impurities, especially that of SiO_2 (25–31 wt.%). Synthetic samples SynCCM-1 and SynCCM-2 exhibited the lowest SiO_2 content. Olivine due to its nature consisted mainly of Mg (46.5 wt.% as MgO), Si (42.9 wt.% as SiO_2) and Fe (8.5 wt.% as Fe_2O_3).

3.1.2. Crystal structure and size

The XRD patterns of representative calcined natural (industrial and laboratory) and synthetic MgOs as well as the olivine sample are shown in Fig. 1. All materials were highly crystalline and exhibited the periclase MgO (cubic) structure while the intensity of the peaks attributed to SiO_2 impurities (quartz hexagonal phase) varied with its content. Such peaks related to impurities were absent from the patterns of the synthetic CCMs. In the DBM samples, the forsterite Mg_2SiO_4 mixed phase was also detected due to the high calcination temperature (>1800 °C) that was applied for the production of these materials. The pattern of olivine was typical of such type of material, showing the presence of various phases, such as forsterite, antigorite, enstatite and talc.

The average crystal size of the natural MgO catalysts was determined by the Scherrer equation using the XRD data of the peak at $2\theta = 42.9^\circ$ and the obtained results are shown in Table 1. The calcination conditions (temperature and duration) of the raw magnesite samples were of vital importance for the crystal morphology and the textural characteristics of the produced MgO catalysts, as was also shown previously [26]. Depending on the calcination process of magnesite, the crystal size of the final MgO catalysts varied between 8 and 70 nm. More specifically, calcination at higher temperature and for longer duration resulted in enhanced sintering of the crystals and consequently, larger crystal sizes were measured. This can be seen by comparing the crystal sizes of the laboratory samples produced from Raw-1, where the crystal size increases in the order of LabCCM–2 > LabCCM–1 > LabCCM–7 > LabCCM-3 in accordance with the increased calcination severity. Similar effect was observed for the two synthetic MgOs (SynCCM-1 and SynCCM-2) obtained by calcination of $Mg(OH)_2$. Among the industrial samples (IndCCMs), the smaller average crystal size (~20 nm) was observed for IndCCM-1, which was derived from the high purity magnesite sample after calcination at relatively mild conditions. On the other hand, the severely calcined DBM samples exhibited much larger crystal size, of ca. 70–80 nm.

The average crystal size was also determined for selected materials before re-calcination at 500 °C for 3 h, in order to study the effect of this stabilization procedure prior to catalytic testing on the textural characteristics of the MgO catalysts. In the case of the industrial samples (IndCCM and DBM), the laboratory calcined samples (LabCCM) and the synthetic SynCCM-1 sample (which was calcined at 1200 °C), no major deference in crystal size values was noticed, implying the high thermal stability of these catalysts due to the severe calcination conditions applied for their production. On the other hand, the synthetic sample SynCCM-2, which was initially calcined at relatively mild conditions, exhibited increased crystal size after re-calcination.

Table 2
Porosity characteristics of MgO and olivine catalysts.

Catalyst	Total SSA[a] (m^2/g)	Total pore volume[b] (ml/g)	Textural/inter-crystal/particle volume[c] (ml/g)	Average pore diameter[d] (nm)
IndCCM-1	64	0.36	0.07	28.9
IndCCM-2	63	0.37	0.11	29.5
IndCCM-3	40	0.34	0.14	34.9
IndCCM-4	20	0.19	0.13	44.1
IndCCM-5	35	0.25	0.11	34.5
DBM-1	0.05	0.01	0.01	–
DBM-2	0.5	0.01	0.01	–
Olivine	1.0	0.01	0.002	–
LabCCM-1	52	0.36	0.08	28.9
LabCCM-2	32	0.28	0.13	34.8
LabCCM-3	113	0.39	0.06	10.0
LabCCM-4	65	0.27	0.05	12.9
LabCCM-5	41	0.28	0.08	23.5
LabCCM-6	25	0.23	0.12	45.0
LabCCM-7	55	0.34	0.06	23.4
SynCCM-1	14	0.27	0.23	91.6
SynCCM-2	56	0.67	0.43	60

[a] From multi-point BET method; t-plot method analysis revealed the absence of microporosity in the solids.
[b] Determined at $P/P_o = 0.99$.
[c] Textural volume = Total pore volume – volume corresponding to $P/P_o = 0.95$.
[d] From BJH analysis using adsorption data.

3.1.3. Porosity characteristics

The nitrogen adsorption–desorption isotherms and the respective pore size distribution curves of representative MgO catalysts studied are shown in Fig. 2 while the surface area, total pore volume, textural (inter-crystal/particle) pore volume and average pore size data are presented in Table 2.

The t-plot analysis of the adsorption data did not reveal the presence of microporosity in the MgO materials, except in the case of SynCCM-1 (which was very low). The adsorption isotherms of the industrial MgO catalysts (IndCCM) are of type II (IUPAC classification), showing relatively narrow hysteresis loops, typical of non-porous materials or materials with high textural porosity originating from inter-crystal/particle voids at the meso/macroporous scale [27]. Indeed, the microporous area/volume (t-plot analysis) of the catalysts was negligible and the measured surface area (20–64 m^2/g) was solely attributed to inter-crystal/particle meso/macropores with average diameters of ca. 29–44 nm (Table 2). Furthermore, by comparing the crystal size data (Table 1) with the porosity data, it can be seen that the decrease of crystal size is accompanied by increase of surface area, as it is depicted in the curve of Fig. 3. This can be attributed both to the higher external surface of smaller crystals as well as to the formation of more confined spaces/voids between them, in the size range of mesopores. The porosity characteristics of DBM were very poor as expected due to its large crystals, while the same stands for olivine due to the morphology of this ore (Table 2).

For the laboratory calcined MgOs, the nitrogen adsorption isotherms of the less severely calcined samples were of the IV type, as can be seen for samples LabCCM-3 and LabCCM-4 in Fig. 2, typical for mesoporous materials with relatively ordered mesopore structure and similar pore size. This is also revealed by the relatively narrow pore size distribution of LabCCM-3, with an average pore size of 10 nm, compared to the rest of the samples (Fig. 2). However, at more intense calcination conditions the isotherms adopted the II type (as can be seen for LabCCM-6), similar to the isotherms of the industrial IndCCM samples. The surface area of the laboratory samples was in the range of 25–113 m^2/g, attributed solely to meso/macropores (10–45 nm) and external surface, as for the industrial samples. The correlation of the crystal size of the laboratory samples with their surface area follows the same trend as for the industrial samples (Fig. 3).

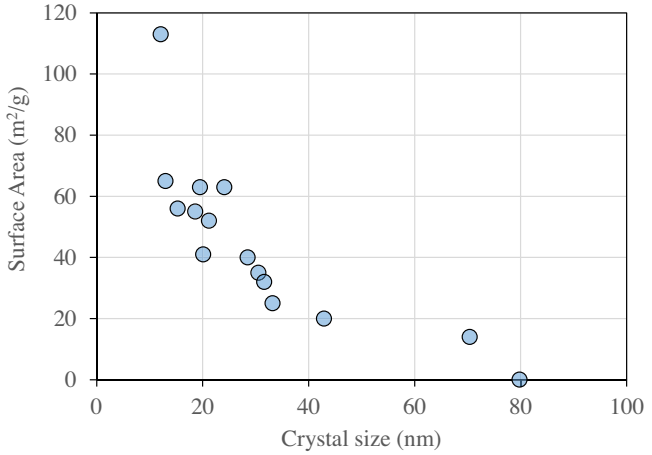

Fig. 3. Specific surface area (BET method, N_2 sorption) of MgO catalysts versus calculated average crystal size (XRD data, Scherrer equation).

The synthetic MgOs, despite being of very high purity, exhibited relatively low surface area and larger pore size compared to the natural MgOs, for similar calcination conditions (*i.e.* compare SynCCM-1 with IndCCM-1, IndCCM-3 or LabCCM-2). In addition, when the sample SynCCM-2, which was produced by mild calcination (500 °C max.), was subjected to the re-calcination/stabilization procedure, its surface area dropped from 153 m^2/g to 56 m^2/g, in accordance to the changes observed in the crystal size (Table 1). However, an interesting feature of this sample was its high textural porosity as can be seen by the pronounced N_2 uptake at $P/Po > 0.95$ (Fig. 2, Table 2).

3.1.4. Morphology (SEM) and structure (HR-TEM)

The morphology of the MgO particles was studied by SEM experiments. Images of representative natural and synthetic MgOs, as well as of olivine are shown in Fig. 4.

The raw magnesite comprises of monolithic or agglomerated plate-like particles of irregular shape but with well-defined facets and edges and with sizes of 0.5–5 μm. Larger aggregates of 10–20 μm can be also seen. The morphology of the particles of IndCCM-1, which was produced by calcination under relatively mild industrial conditions, has been changed to a more rounded shape and with sponge-like texture, having similar sizes (ca. 0.5–5 μm) to those of parent magnesite particles. Larger aggregates of up to 10–20 μm were also observed in this sample. On the other hand, the morphology and texture of the severely calcined DBM particles resemble those of the raw magnesite, having smooth well-defined facets and edges and adopting in some cases clear cubic or orthogonal parallelepiped shapes (Fig. 4). In addition, the size of these monolithic or agglomerated particles are larger, due to the advanced sintering in accordance with their larger crystal sizes (XRD data), mostly in the range of 5–20 μm, with some particles as large as 50–150 μm. This dense texture of the DBM particles, in contrast to the more sponge-like morphology of the IndCCM particles, is in line with the almost negligible porosity of the former materials (Table 2). The non-porous nature of the olivine particles can be also confirmed by its large monolithic/agglomerated particles shown in the respective SEM images. In the case of the more mildly calcined laboratory samples (LabCCM-3), the particles exhibit a morphology similar to that of IndCCM-1 (the less intensively treated industrial material), with rounded particles of smaller size, mostly in the range of 0.1–3.5 μm (Fig. 4). Few aggregated particles of < 10 μm are also observed. The particles of synthetic MgO (SynCCM-2) which has been mildly calcined have the same morphology and spongy texture as those of LabCCM-3 with even smaller size of 0.1–2 μm,

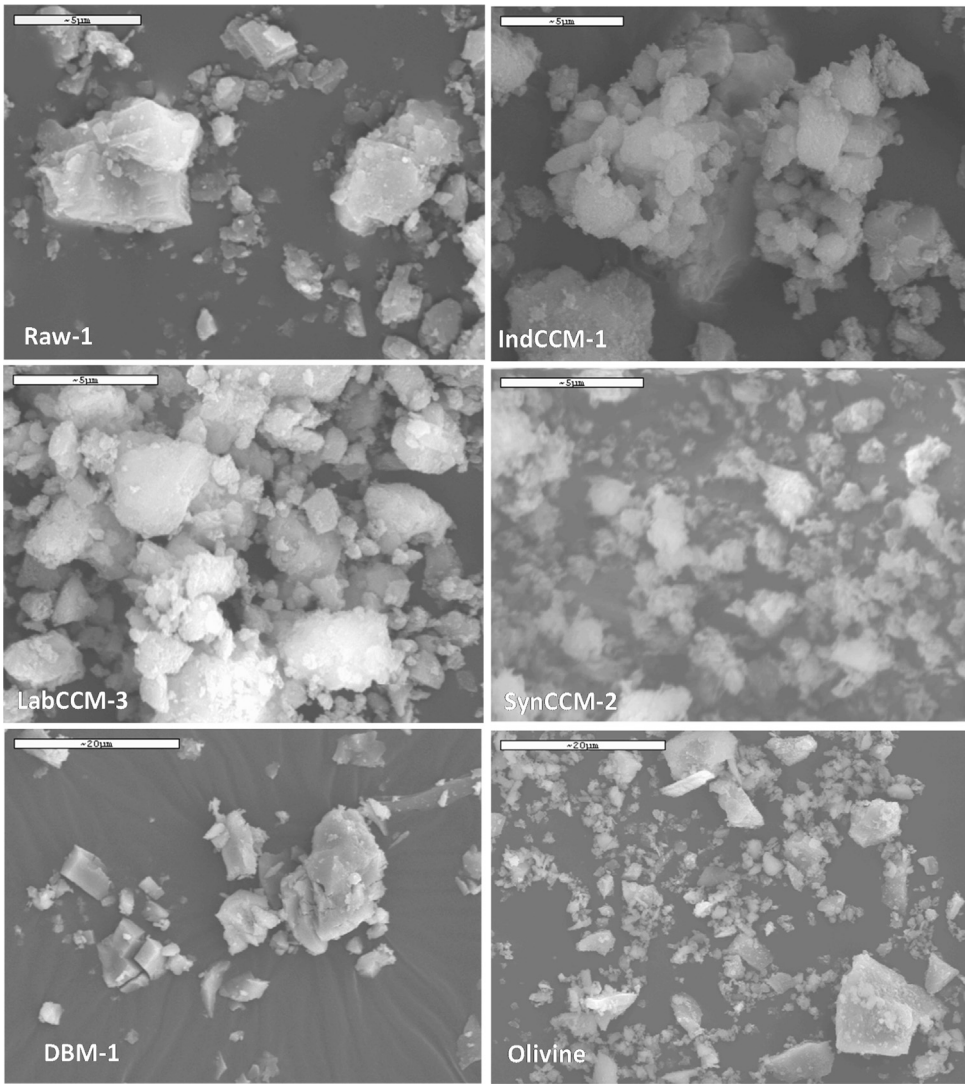

Fig. 4. Representative SEM images of magnesite (Raw-1), industrially produced natural MgOs (IndCCM-1, DBM), laboratory produced natural MgO (LabCCM-3), synthetic MgO (SynCCM-2), and of olivine (scale bars are 5 μm, except that for olivine and DBM-1 which are 20 μm).

and aggregates smaller than ca. 5 μm (Fig. 4). This morphology justifies the high textural porosity of this catalyst as discussed above (data in Table 2 and Fig. 2).

The morphology of crystals at the nanoscale was studied by HR-TEM experiments. The natural MgO sample IndCCM-1 that was produced by calcination under relatively mild industrial conditions comprised of nanocrystals with square or rectangular shape and sizes of ca. 10–80 nm, the majority being in the range of 20–30 nm (Fig. 5a), in accordance with the average crystal size estimated by the XRD data and Scherrer equation (~20 nm). The nanocrystals were either as individual crystals or partially agglomerated at their edges. The Selected Area Diffraction (SAD) measurements of the individual crystals (inset in the image of IncCCM-1 in Fig. 5a) verified that these are single crystals and the observed reflections corresponded to the {111} and {200} crystallographic planes, typical of the cubic structure of MgO. The average distance between the {200} lattice fringes shown in the high resolution image of a selected crystal in Fig. 5b, was 0.211 nm, which corresponds to a lattice constant of a = 0.422 nm (being similar to that of MgO periclase cubic structure, a = 0.421 nm).

The sample that was produced *via* more intense industrial calcination conditions, *i.e.* IndCCM-4, comprised of crystals with rectangular shape and sizes mostly in the range of 30–80 nm (the average crystal size from XRD data being ~43 nm), forming also larger agglomerates up to ca. 500 nm (Fig. 5c). The SAD patterns of the individual crystals (inset in Fig. 5c) revealed also the presence of {111} and {200} crystallographic planes, as in the case of IndCCM-1. A different nanoparticle morphology was observed for the synthetic MgOs, as can be seen in Fig. 5d, for the mildly calcined SynCCM-2 sample. The primary nanoparticles had irregular shapes and small sizes of ca. < 20 nm, which were in most cases agglomerated to bigger particles/assemblies with internal narrow voids resembling a solid with high textural/inter-particle meso/macroporosity. In addition to these assemblies, the sample comprised of nanorods with ~5 nm width which are agglomerated to larger rod-like particles with dimensions of 20–50 nm wide and up to ca. 500 nm long. The high resolution measurements and the SAD patterns showed that both the nanoparticle assemblies and the nanorods exhibit the crystalline structure of MgO with, however, reduced crystallinity. For this reason multiple reflections were observed in the SAD patterns, mainly of the {200} type (inset in Fig. 5d). Still, the determined lattice constant was a = 0.419 nm, in very good agreement with the theoretical value for MgO.

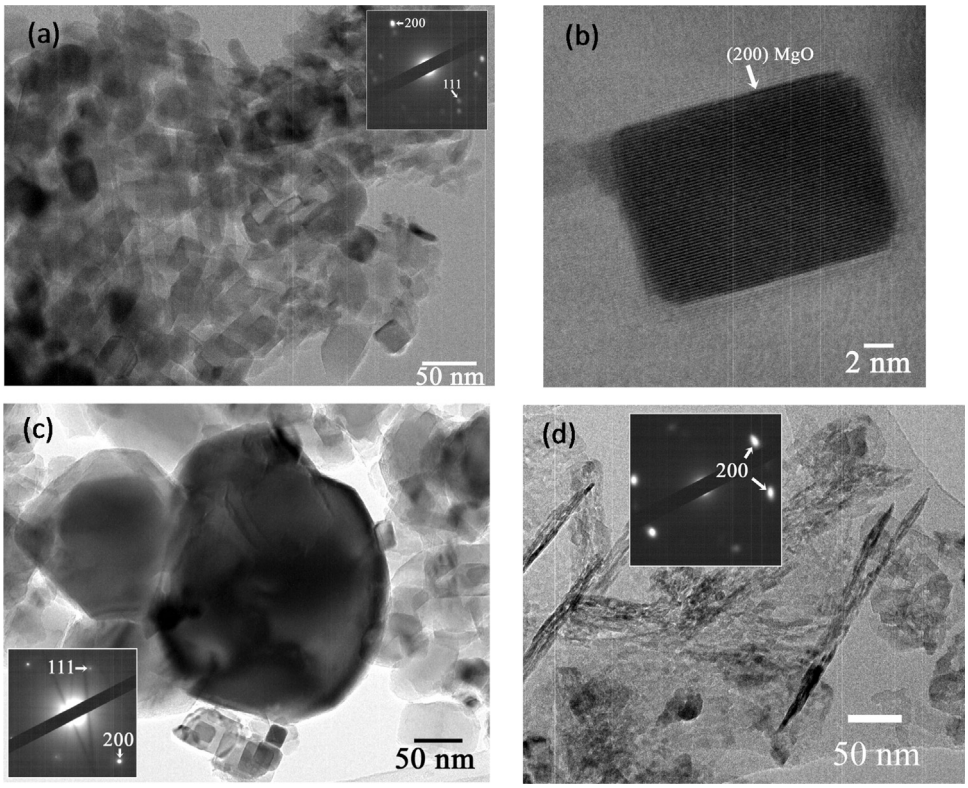

Fig. 5. TEM images of (a) natural MgO IndCCM-1, (b) single crystal of IndCCM-1, (c) natural MgO IndCCM-4, and (d) synthetic MgO SynCCM-2. The insets in all images show the electron diffraction pattern (Selected Area Diffraction pattern, SAD) derived from the corresponding region of the particles.

3.1.5. Basicity and acidity

The basicity of the MgO catalysts was measured with TPD-CO_2 experiments. The TPD-CO_2 curves are presented in Fig. 6, while the total number of basic sites (total basicity), the number of weak/medium and strong basic sites, the ratio between them and the temperature maxima of the respective TPD-CO_2 peaks are shown in Table 3.

The TPD-CO_2 curves of all natural CCMs (both industrial and laboratory) exhibited two main peaks; the first between 100 and 400 °C (with maxima in the range of 200–260 °C) attributed to weak/medium basic sites and the second between 450 and 600 °C (with maxima in the range of 500–570 °C) attributed to strong basic sites. Depending on the crystal size, surface area and chemical composition, the number of basic sites of the IndCCMs fluctuated from 2 up to 244 μmol CO_2/g, which are in the range of values reported previously for various laboratory synthetic and commercial MgOs [28–30]. IndCCM-1 exhibited the highest total number of basic sites due to its high Mg content, small crystal size and relatively high surface area (Tables 1, 2 and 3). However, samples still exhibiting relatively high purity but reduced surface area (IndCCM-3 and IndCCM-5), had lower number of basic sites (both weak/medium and strong), thus indicating the positive effect of higher surface area due to the enhanced accessibility of active basic MgO sites. In all the above high purity MgO samples, the ratio of strong to weak/medium basic sites was relatively low (0.2–0.3), as can be seen in Table 3. On the other hand, IndCCM-2 and IndCCM-4, derived from calcination of a moderate purity magnesite, had a larger portion (higher than 50%) of strong basic sites, probably due to the high amount of impurities, especially CaO (up to 2.4 wt.%), which can provide strong basic sites. In addition, the significantly lower surface area of IndCCM-4 induced a pronounced decrease of the weak/medium sites attributed mainly to MgO, thus resulting to a higher strong to weak/medium ratio of about 1. Accordingly, the DBM and olivine samples had very low number of basic sites due to their negligible surface area. Previous studies on the basicity of MgOs have reported similar TPD-CO_2 curves, at least for desorption temperatures up to ca. 500 °C [30–32]. Basic sites of weak/medium strength (with maxima of ca. 200 °C) were attributed to Mg^{2+}–O^{2-} ion pairs while isolated O^{2-} anions were suggested as the source of higher strength sites (with maxima higher than ca. 300 °C).[30] However, the clear peaks with maxima in the range of 500–570 °C shown in Fig. 6 for the natural MgOs, have not been previously identified, and may indicate the presence of very strong basicity.

Similar observations were made for the samples calcined in the laboratory (Fig. 6b), with those of relatively high surface area and purity (LabCCM-1, 3 and 7) exhibiting the higher number of weak/medium (and total) number of basic sites and relatively low ratio of strong to weak/medium strength sites (Table 3). On the other hand, the low purity samples, especially those with decreased surface area (LabCCM-5 and 6), possess markedly lower number of weak/medium basic sites and relatively high portion of strong sites due to the presence of impurities. The two synthetic CCMs exhibited very low number of weak/medium basic sites, possibly due to their different morphology and low crystallinity (HRTEM data), in comparison to the well-formed crystals of the natural calcined MgOs. Furthermore, the synthetic MgOs exhibit two relatively distinct peaks at ~175 °C and ~275 °C (Fig. 6b), being attributed to sites of different (moderate) strength, as was also previously reported [30]. The complete absence of strong basic sites (*i.e.* corresponding to TPD-CO_2 peaks with maxima > 500 °C) in the synthetic MgOs can be attributed to the very low content of impurities (*i.e.* CaO).

As expected in Ref. [33], the MgO catalysts exhibited negligible acidity (*i.e.* <13 μmoles NH_3/g, see Table 3), all of which were

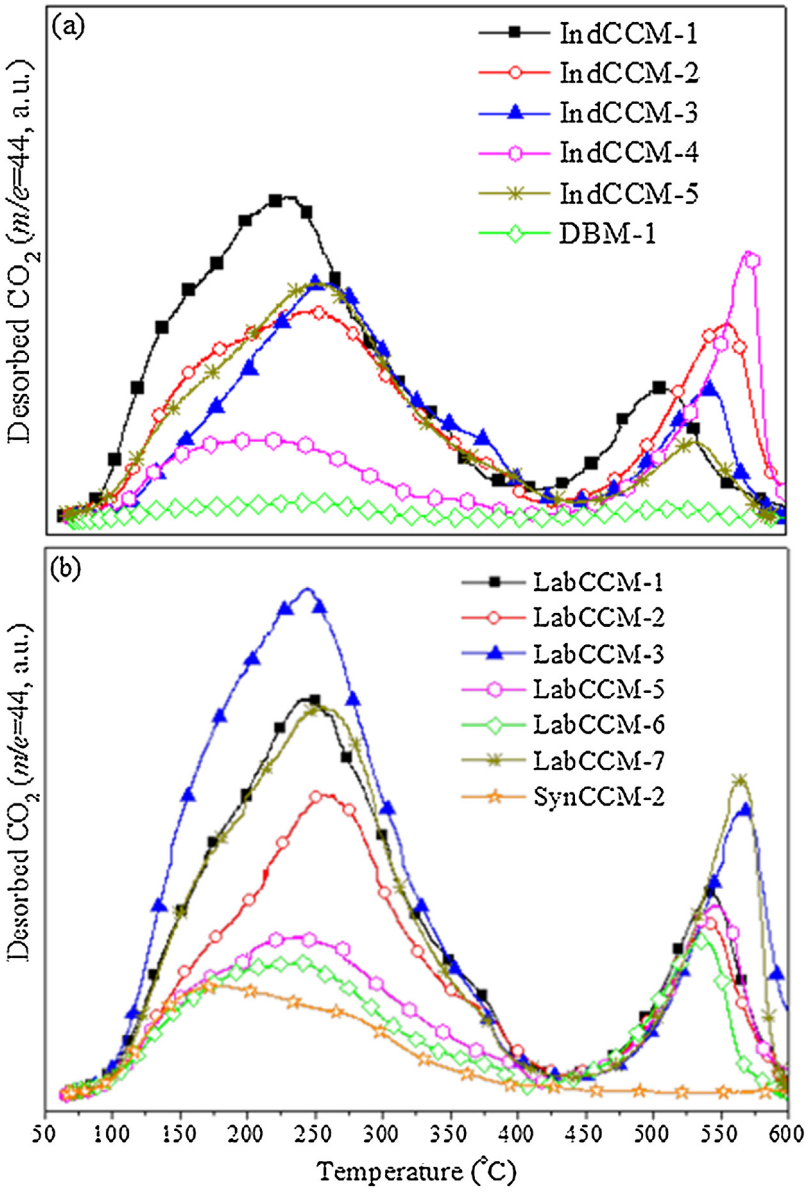

Fig. 6. TPD-CO_2 curves of (a) natural MgOs caclined under industrial conditions (IndCCM and DBM) and (b) natural (laboratory calcined, LabCCM) and synthetic (SynCCM) MgOs.

Table 3
Acidity and basicity of MgO and olivine catalysts.

Sample	Acidity (μmol NH_3/g)	Basicity (μmol CO_2/g)	Week/medium basic sites (μmol/g)	T_{max}. weak/medium basic sites (°C)[a]	Strong basic sites (μmol/g)	T_{max}. strong basic sites (°C)[b]	Ratio of Strong to Weak/medium basic sites
IndCCM-1	2.5	244	200	225	44	500	0.2
IndCCM-2	0.5	133	86	248	47	558	0.6
IndCCM-3	2.1	147	115	256	32	544	0.3
IndCCM-4	–	77	38	204	39	571	1.0
IndCCM-5	–	122	100	252	22	532	0.2
DBM-1	–	9.4	6.2	246	3.2	516	0.5
Olivine	3.1	1.9	1.0	–	0.9	–	1.0
LabCCM-1	12.9	192	150	245	42	543	0.3
LabCCM-2	8.1	147	109	258	38	540	0.3
LabCCM-3	2.9	230	159	245	72	566	0.5
LabCCM-4	–	206	124	240	82	569	0.7
LabCCM-5	4.6	95	57	238	38	547	0.7
LabCCM-6	–	81	54	238	27	537	0.5
LabCCM-7	4.5	207	153	256	54	564	0.3
SynCCM-1	4.3	25	25	161/304	0	–	–
SynCCM-2	4.9	49	49	179/276	0	–	–

[a] Temperature of peak maximum of the TPD curve in the region of 50–450 °C.
[b] Temperature of peak maximum of the TPD curve in the region of 450–600 °C.

Table 4
Product yields (wt.% on biomass) in the non-catalytic and catalytic pyrolysis of lignocellulosic biomass with the MgO and olivine catalysts.

Catalyst	Bio-oil[a]	Water[b]	Organics[c]	Gases	Solids[d]
Non Catalytic	61.3	22.4	38.9	17.4	21.3
ZSM-5	49.2	28.5	20.7	24.7	26.0
IndCCM-1	44.1	26.2	17.8	27.2	28.7
IndCCM-2	46.5	27.1	19.4	24.0	29.5
IndCCM-3	50.3	28.9	21.3	24.4	25.3
IndCCM-4	52.7	26.9	25.7	22.4	24.9
IndCCM-5	49.5	24.2	25.3	22.8	27.7
LabCCM-1	44.7	25.6	19.1	26.7	28.6
LabCCM-2	47.1	25.9	21.2	24.9	28.1
LabCCM-3	40.3	27.2	13.1	27.6	32.1
LabCCM-4	46.5	26.8	19.7	25.8	27.7
LabCCM-5	44.5	26.1	18.4	26.0	29.6
LabCCM-6	49.3	24.9	24.3	23.8	26.9
LabCCM-7	46.6	24.7	21.9	25.6	27.8
SynCCM-1	49.5	24.8	24.8	23.0	27.5
SynCCM-2	43.8	28.5	15.3	26.0	30.2
DBM-1	61.2	24.2	36.9	17.9	21.0
DBM-2	61.2	23.3	37.9	17.5	21.3
Olivine	57.9	20.8	37.1	17.8	24.3

[a] Total liquid product (pyrolysis oil).
[b] Water content of bio-oil.
[c] Organic phase of bio-oil (total bio-oil minus water).
[d] Char plus catalytic coke.

attributed to Lewis acid sites, as verified by FTIR-pyridine sorption measurements (not shown for brevity).

3.2. *In-situ upgrading of biomass fast pyrolysis vapors*

In a typical catalytic fast pyrolysis process (or also named as *in situ* catalytic upgrading of biomass fast pyrolysis vapors) the solid biomass initially vaporizes *via* thermal/non-catalytic reactions (*i.e.* hydrolysis, cracking/depolymerization, decarbonylation, decarboxylation and dehydration) and decomposes to smaller fragments or even single molecules, such as levoglucosan, ketones, acids, phenolics, etc. These smaller oligomers/molecules react further on the catalyst active sites *via* a set of reactions (dehydration, decarbonylation, decarboxylation, cracking, ketonization, condensation, dehydrocyclization/aromatization, polymerization/coke formation) depending on the nature of the catalyst, *i.e.* acidic, basic, metallic, etc. In the next paragraphs, a thorough description and discussion of the performance of basic MgO catalysts are presented, in comparison with the more classical acidic ZSM-5 zeolite catalyst.

3.2.1. *Effect of catalyst type on product yields*

The product yields for all the MgO and olivine catalysts tested in the pyrolysis of lignocellulosic (beech wood) biomass is presented in Table 4. The respective data for a ZSM-5 zeolitic catalyst and for the non-catalytic (conducted with inert silica sand) experiment are also included for comparison. The main products obtained were the pyrolysis oil (bio-oil) that comprises of an organic and an aqueous (water) phase, gases (CO, CO_2, H_2 and C_1–C_6 hydrocarbons) and solids (char and catalytic coke).

The changes in the product yields induced by the acidic ZSM-5 zeolitic catalyst compared to the non-catalytic experiment were the expected ones, *i.e.* decrease of the organics through their conversion to water (dehydration), gases (decarbonylation, decarboxylation, cracking) and catalytic coke (aromatization/polymerization reactions, as explained below). The changes in the yields were not as high as those reported in previous works [34,35], since the zeolitic catalyst used in the present study was an industrial ZSM-5 based formulation that consisted of about 30% crystalline zeolite diluted in a silica-alumina matrix. The acidic properties of this catalyst were inferior to those of a pure ZSM-5 zeolite (*i.e.* 36.5 versus 113.8 μmoles of Brønsted acid sites/g catalyst as determined by FTIR-pyridine sorption experiments [35]). As a result, its acid reactivity and the respective effect on the product yields in biomass pyrolysis were not as pronounced as they were with the pure ZSM-5 [35]. However, such catalytic formulations consisting of the active zeolite and a matrix/binder are more representative of a potential industrial catalyst that could be used in continuous circulated fluid bed pilot or commercial scale reactors for the catalytic fast pyrolysis of biomass [36].

Interestingly, all the natural caustic calcined (IndCCM and LabCCM) and synthetic (SynCCM) MgOs, except the severely calcined DBM materials, showed similar or even higher activity in converting the organics, compared to that of the ZSM-5 catalyst (Table 4). As the MgO catalysts possess only basic sites and negligible (mainly Lewis) acidity, it is expected that different reaction mechanisms prevail leading to altered product yields compared to ZSM-5 zeolite. Indeed, one general observation from the data in Table 4, is that when the MgO catalysts induce the same yield of organics with that of ZSM-5, the water content of bio-oil is slightly less, while the gases and solids (due to reaction coke) are slightly higher with the MgOs (compare data of ZSM-5 with those of IndCCM-1, 2 and LabCCM-1, 2, 4). It is also clear from the data in Table 4 that the higher the surface area of the MgO catalysts the higher their reactivity, with respect to conversion of organics. The LabCCM-3 catalyst (surface area of 113 m^2/g) was the most active and the two DBM catalysts (negligible surface area) exhibited very low activity. The synthetic catalyst SynCCM-2 is the only one that "deviated" from this general trend since it exhibits very high reactivity, still having moderate surface area (56 m^2/g). The significantly high textural porosity and external surface (Table 2, Fig. 2) of this catalyst can be the reason for its high reactivity. Other general observations are that the high ratio of strong to weak/medium basic sites (IndCCM-2, 4 and LabCCM-4, 5) and the presence of high amounts of impurities (LabCCM-4, 5 and 6) did not have a clear effect on reactivity and product yields. The effect of the various physicochemical properties of the MgO catalysts on product yields is also discussed in more detail below.

The difference in the solids yield (Table 4) between the catalytic and the non-catalytic pyrolysis experiments was attributed to the formation of coke on the catalyst (catalytic coke), as the char formed was practically the same in all experiments, according to the design of our experimental setup. Coke is undesirable because it blocks the catalyst's pores and active sites leading to deactivation, while on the other hand, it binds biomass carbon on the catalyst, thus lowering the bio-oil yield and its calorific value [14]. However, coke can be utilized in a continuous process like the circulating fluid bed operation when it is burned in the regenerator to provide heat for the process [36]. Coke can tentatively be formed *via* oligomerization, cyclization, hydrogen transfer and condensation reactions that are being catalyzed by the catalyst's acid sites to form polycyclic aromatic hydrocarbons from olefins and monocyclic hydrocarbons [37–39]. Coke can also be tentatively formed by aldol condensation and Diels-Alder reactions of oxygenated compounds towards large molecules that are deposited on the catalyst surface [21,39]. Since the basic MgO catalysts had very low acidity (Table 3), reduced coke formation was expected. However, most of the MgO catalysts yielded similar or even higher coke to that produced by the ZSM-5 catalyst when compared at similar yield of organics (compare data of ZSM-5 with those of IndCCM-1, 2 and LabCCM-1, 2, 4 in Table 4). Coke formation was tentatively facilitated by the large mesopores present in the MgOs (Table 2), which allowed the condensation and further polymerization of oxygenates, such as ketones, and the formation of larger oxygenated molecules that contributed to coke. The initial formation of ketones is favored on the basic sites of the MgO catalysts in contrast to the formation of aromatics on the acid sites of ZSM-5, as is discussed below, thus minimizing the formation of polycyclic aromatic hydrocarbons (PAHs) and

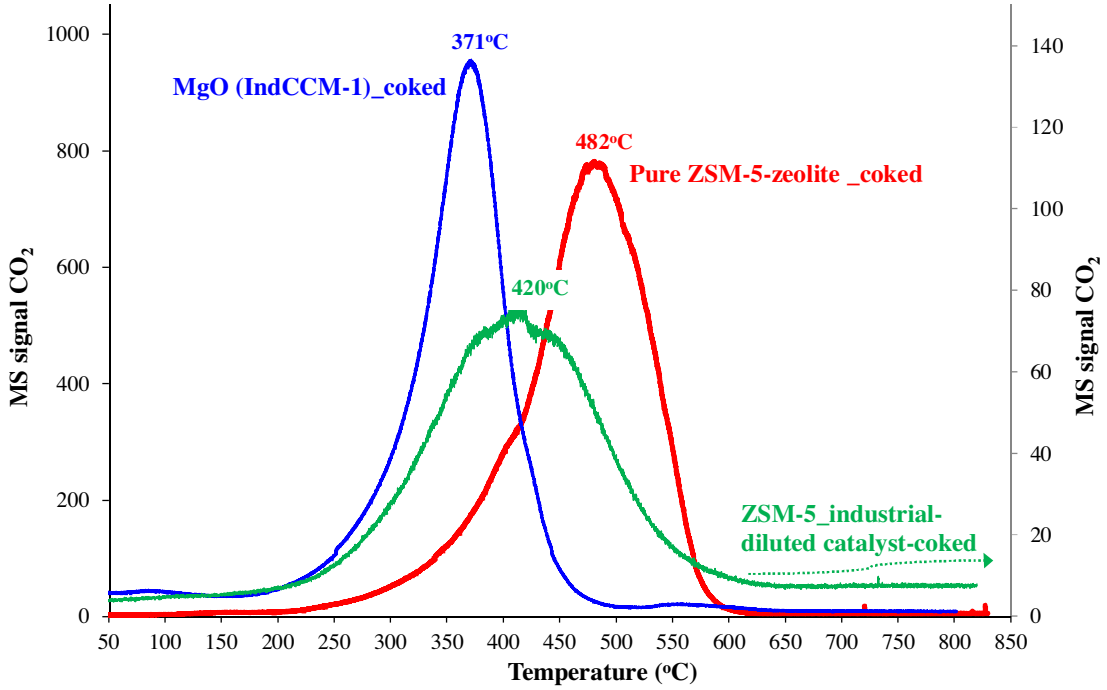

Fig. 7. Temperature programmed oxidation (TPO) curves of coked catalysts after catalytic biomass fast pyrolysis experiments, monitoring the production of CO_2 ($m/z = 44$). A coked sample of pure H-ZSM-5 zeolite (Zeolyst, CBV 8014, Si/Al = 40) was also included for comparison with the natural MgO and the industrial diluted ZSM-5 catalyst formulation.

coke originating from PAHs. Preliminary thermogravimetric analysis (TGA) measurements in combination with elemental analysis (C,H,O) have shown that the catalytic coke formed on the MgOs is slightly more oxygenated compared to that deposited on ZSM-5 zeolite catalyst. In addition, temperature programmed oxidation (TPO) results of the used catalysts have shown that the coke formed on MgOs is more "soft", as is being oxidized/burnt at lower temperatures, compared to the "harder" coke of ZSM-5 catalysts, as shown in Fig. 7.

Consequently, the natural MgO catalysts, which have been produced under industrial conditions, were easily regenerated by simple calcination in air at ca. 500 °C, without any significant changes of their textural, basic and catalytic properties. However, a more systematic study of coke nature and formation mechanism over the MgO catalysts is still required.

3.2.2. *Effect of catalyst type on gas composition*

The detailed gas yields for each catalyst tested are presented in Table 5. Gases were composed primarily of CO_2 and CO. Hydrogen and light hydrocarbons with up to 6 carbon atoms were also present but in smaller quantities. It is interesting to note that during the catalytic pyrolysis with the acidic ZSM-5, the increase in the gas products compared to the non-catalytic pyrolysis was mainly due to higher CO production, while the CO_2 yield was not substantially increased. On the other hand, in the catalytic pyrolysis with the basic MgO catalysts (except DBM-1, DBM-2 and olivine, which exhibited very low reactivity), the increase in the CO_2 yield was greater than that of the CO yield. With the formation of CO_2, two oxygen atoms are being removed from the liquid pyrolysis products for every carbon atom that ends up in the gases, while with the formation of CO only one oxygen atom is removed. Thus, the formation of CO_2 is more preferable for the efficient production of deoxygenated bio-oil and based on the data of Table 5, it was clearly favored by the use of basic MgO catalysts. Light hydrocarbon gas yields also increased by the use of MgO catalysts (except in the cases of DBM-1, DBM-2 and olivine), indicating enhanced thermal cracking of the pyrolysis vapors.

Table 5
Gas product yields (wt.% on biomass) in the non-catalytic and catalytic pyrolysis of lignocellulosic biomass with the MgO and olivine catalysts.

Catalyst	CO_2	CO	H_2	CH_4	C_2H_6	C_2H_4	C_3H_8	C_3H_6	C_4–C_6
Non Catalytic	9.3	6.4	0.0	0.9	0.2	0.2	0.0	0.1	0.2
ZSM-5	10.5	10.8	0.0	1.0	0.2	0.6	0.1	0.7	0.8
IndCCM-1	14.4	9.3	0.1	1.6	0.3	0.3	0.1	0.3	0.8
IndCCM-2	12.6	8.2	0.1	1.4	0.3	0.3	0.1	0.3	0.8
IndCCM-3	13.2	8.3	0.1	1.4	0.3	0.3	0.1	0.2	0.6
IndCCM-4	12.0	7.9	0.0	1.2	0.2	0.3	0.1	0.2	0.5
IndCCM-5	12.4	7.9	0.0	1.2	0.2	0.2	0.1	0.2	0.5
LabCCM-1	14.0	9.1	0.1	1.5	0.3	0.3	0.1	0.3	0.9
LabCCM-2	13.3	8.5	0.0	1.4	0.3	0.3	0.1	0.2	0.7
LabCCM-3	14.8	9.0	0.1	1.6	0.4	0.3	0.1	0.3	1.0
LabCCM-4	13.8	8.7	0.1	1.5	0.3	0.3	0.1	0.3	0.9
LabCCM-5	13.9	8.8	0.1	1.5	0.3	0.3	0.1	0.3	0.7
LabCCM-6	12.9	8.3	0.1	1.3	0.3	0.3	0.1	0.2	0.5
LabCCM-7	13.6	8.9	0.1	1.5	0.3	0.3	0.1	0.3	0.7
SynCCM-1	12.4	7.9	0.0	1.2	0.2	0.3	0.1	0.2	0.6
SynCCM-2	13.7	8.7	0.1	1.6	0.4	0.3	0.1	0.3	0.9
DBM-1	9.5	6.5	0.0	0.9	0.2	0.2	0.0	0.1	0.3
DBM-2	9.4	6.4	0.0	0.9	0.2	0.2	0.0	0.1	0.3
Olivine	9.8	6.3	0.0	0.9	0.2	0.2	0.0	0.1	0.3

3.2.3. *Catalyst influence on bio-oil oxygen content*

In Fig. 8, the yield of organic fraction of the bio-oil obtained for each catalyst is plotted against its oxygen content. The corresponding data for the non-catalytic pyrolysis and the experiments with the ZSM-5 catalyst are highlighted as reference points. As shown, the oxygen content of the bio-oil's organic fraction was reduced with all catalytic materials tested. In the case of the acidic ZSM-5 zeolite, it was reduced from ~39 wt.% (in non-catalytic bio-oil) to 31 wt.% with a subsequent decrease of the organic fraction yield from 39 wt.% to 20.7 wt.%, due to the removal of oxygen and the increased formation of gas products, water and catalytic coke, as

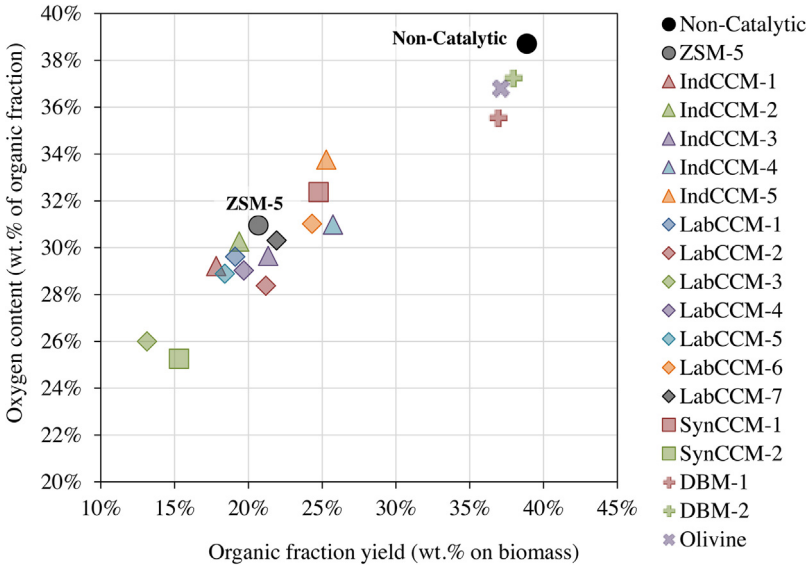

Fig. 8. Organic fraction yield vs. oxygen content in the organic fraction of bio-oil for all the MgO and olivine catalysts tested. Zeolite ZSM-5 and non-catalytic data are included for comparison.

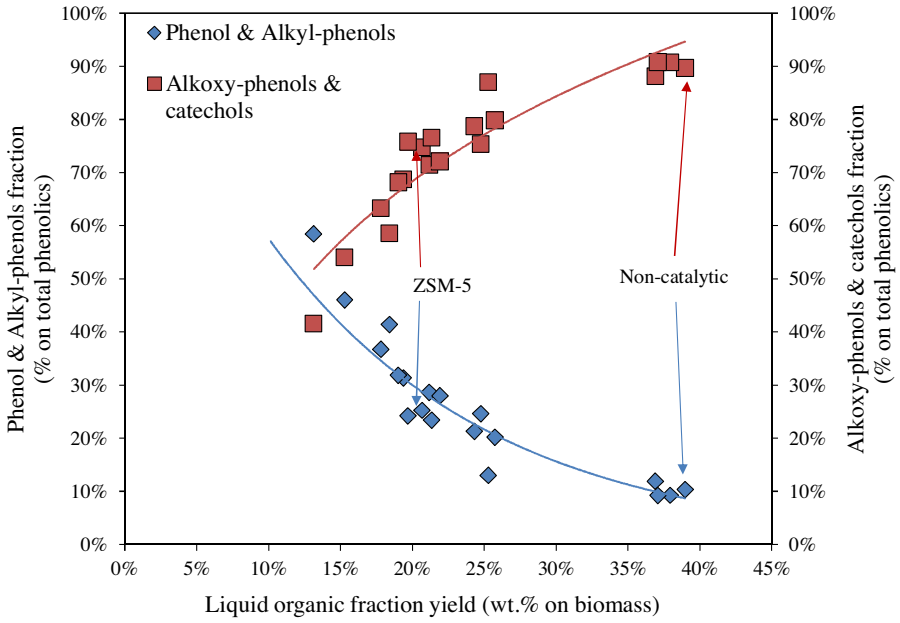

Fig. 9. Relative abundance of phenols without oxygenated substitutes (phenol plus alkyl-phenols) and oxygenated phenolics (alkoxy-phenols plus catechols) versus bio-oil's organic fraction yield.

described above. The natural MgO catalysts had a similar effect and reduced the oxygen content in the organic fraction, while also decreasing the organic fraction yield. The degree of deoxygenation depended on the properties of the materials; less active catalysts with poor porosity and textural properties (DBM-1, DBM-2 and Olivine) induced minimal deoxygenation, while catalysts with high surface area and/or high external surface (LabCCM-3 and SynCCM-2, respectively) provided the lowest oxygen content, albeit with a significant reduction in the organic fraction.

Compared to the more commonly used ZSM-5, the natural MgO catalysts of the present study showed very promising results. Specifically, the IndCCM-4 and LabCCM-6 catalysts yielded substantially more organic fraction (24.3–25.7 wt.% on biomass) than the ZSM-5 catalyst (20.7 wt.% on biomass) while reducing the oxygen content to 30–31 wt.%, thus producing bio-oil of comparable quality with that of ZSM-5. Furthermore, the LabCCM-2, LabCCM-4 and LabCCM-5 catalysts produced bio-oil with a marked reduction in the organic fraction's oxygen content (about 28–29 wt.%), while maintaining the organic fraction yield (in the range of 18.4–21.2 wt.% on biomass) at levels comparable to those of ZSM-5 (20.7 wt.% on biomass). Thus, the natural MgO materials can be considered as promising catalysts for the catalytic pyrolysis of biomass

Table 6
Bio-oil composition obtained with the MgO and olivine catalysts (GC–MS area%).

Catalyst	AR	ALI	PH	FUR	AC	EST	AL	ETH	ALD	KET	PAH	SUG	NIT	UN
Non Catalytic	0.0	0.0	28.0	0.0	19.2	0.0	0.0	1.8	0.3	5.0	0.0	0.1	0.2	40.2
ZSM-5	5.1	0.4	35.4	0.8	7.4	0.0	0.3	4.8	0.6	3.3	1.8	0.0	0.4	39.7
IndCCM-1	0.9	0.8	36.1	0.7	11.3	0.2	0.5	0.4	0.6	8.2	0.1	0.0	0.1	40.1
IndCCM-2	0.4	0.6	36.7	0.5	10.3	0.0	0.1	0.1	2.7	7.1	0.0	0.0	0.1	41.4
IndCCM-3	0.6	0.2	40.0	0.4	9.7	0.3	0.0	0.8	0.6	10.1	0.1	0.0	0.3	36.8
IndCCM-4	0.3	0.1	35.2	0.3	11.8	0.0	0.0	0.7	0.6	8.6	0.1	0.0	0.7	41.6
LabCCM-1	0.2	0.4	34.0	0.8	11.2	0.0	0.0	0.0	2.1	7.3	0.0	0.0	0.6	43.3
LabCCM-2	0.5	0.2	32.1	1.0	9.3	0.0	0.0	2.7	1.1	9.6	0.0	0.0	0.7	42.8
LabCCM-3	1.2	1.1	31.7	1.1	5.5	0.2	1.4	1.1	0.0	9.7	0.5	0.0	0.0	46.3
LabCCM-4	0.3	0.2	36.2	0.6	10.9	0.0	0.0	0.0	0.8	4.8	0.0	0.0	0.1	46.1
LabCCM-5	0.3	0.0	31.2	0.9	9.3	0.0	0.3	1.4	0.9	7.1	0.4	0.0	1.9	46.2
LabCCM-6	0.5	0.5	28.5	0.3	11.6	0.0	1.8	3.0	0.8	6.8	0.0	0.0	1.7	44.5
LabCCM-7	0.5	0.0	32.4	0.3	13.4	0.0	0.0	0.1	1.6	6.6	0.2	0.0	0.5	44.3
IndCCM-5	0.7	0.1	35.7	0.2	14.1	0.0	0.0	0.2	1.2	6.2	0.2	0.0	0.1	41.4
SynCCM-1	0.5	0.3	31.2	1.2	9.4	0.0	0.0	2.1	1.1	9.4	0.0	0.0	0.0	44.7
SynCCM-2	0.7	0.4	29.9	0.5	9.5	0.0	0.3	0.2	0.9	9.7	0.4	0.0	0.0	47.4
DBM-1	0.0	0.1	27.3	0.0	16.3	0.0	0.0	3.8	0.5	4.8	0.0	0.0	0.0	47.2
DBM-2	0.0	0.0	27.2	0.0	17.8	0.0	0.0	2.1	0.3	4.6	0.0	0.1	0.2	47.8
Olivine	0.3	0.0	35.1	0.0	16.8	0.0	0.1	0.0	0.8	6.9	0.0	0.0	0.1	39.7

Table 7
Most abundant compounds in non-catalytic and catalytic bio-oil of representative MgO catalysts.

	Non-catalytic	ZSM-5	IndCCM-1	LabCCM-3	SynCCM-2	IndCCM-5
Acids						
Acetic acid	15.0	6.4	11.3	5.5	5.0	13.4
3,5-Dimethoxy-4-hydroxyphenylacetic acid	1.1	0.8	0.0	0.0	0.0	0.7
Benzoic acid, 4-hydroxy-3-methoxy-	3.1	0.0	0.0	0.0	0.0	0.0
Aromatics						
Toluene	0.0	0.6	0.1	0.0	0.4	0.2
Indene	0.0	0.5	0.0	0.2	0.2	0.0
2-Methylindene	0.0	0.4	0.1	0.1	0.0	0.0
1H-Indene, 1,3-dimethyl-	0.0	0.4	0.0	0.0	0.0	0.0
Aliphatics						
1-Methylcycloheptene	0.0	0.0	0.6	0.0	0.5	0.0
6-Methyl-3-heptyne	0.0	0.0	0.0	0.8	0.3	0.0
Furans						
Benzofuran, 2-methyl-	0.0	0.5	0.3	0.7	0.4	0.2
Benzofuran, 7-methyl-	0.0	0.4	0.2	0.2	0.2	0.0
Aldehydes						
2-Furancarboxaldehyde, 5-methyl-	0.3	0.0	0.6	0.0	0.8	1.2
2-Propenal, 3-phenyl-	0.0	0.5	0.0	0.0	0.0	0.0
Ketones						
2-Cyclopenten-1-one, 2-hydroxy-	2.6	0.0	0.8	0.0	0.0	1.6
2-Cyclopenten-1-one, 2,3-dimethyl-	0.3	0.3	1.6	2.0	1.6	0.7
1,2-Cyclopentanedione, 3-methyl-	1.1	0.8	0.6	0.0	1.2	1.0
2-Cyclopenten-1-one, 2-methyl-	0.0	1.1	2.6	2.3	3.0	1.1
2-Cyclopenten-1-one, 3-methyl-	0.0	0.6	0.6	1.3	1.7	0.0
Acetophenone	0.0	0.0	0.2	0.4	0.0	0.0
Phenol & Alkyl-Phenols						
Phenol	0.4	2.2	1.6	2.4	2.1	0.7
Phenol, 2-methyl-	0.7	1.4	2.2	2.4	2.4	1.3
Phenol, 3-methyl-	0.7	0.0	2.0	3.7	2.8	0.0
Phenol, 2,4-dimethyl-	0.3	0.5	1.9	1.3	1.5	0.8
Phenol, 4-methyl-	0.0	1.7	0.6	0.0	0.3	1.1
Phenol, 3,5-dimethyl-	0.0	0.0	0.4	3.9	0.4	0.0
Alkoxy-Phenols						
Phenol, 2-methoxy-	1.6	2.1	1.9	0.5	1.3	2.2
Phenol, 2-methoxy-4-methyl-	1.3	1.5	1.3	1.0	1.4	1.6
Phenol, 4-ethyl-2-methoxy-	1.3	0.9	1.7	2.2	2.0	2.3
2-Methoxy-4-vinylphenol	1.8	2.2	1.9	0.0	0.0	2.3
Phenol, 2,6-dimethoxy-	4.4	3.1	2.1	0.7	2.0	4.7
Phenol, 3,4-dimethoxy-	1.1	1.2	0.0	0.0	0.0	0.4
Phenol, 2-methoxy-4-(1-propenyl)-, (Z)-	0.4	0.5	1.1	0.0	0.0	0.7
Phenol, 2,6-dimethoxy-4-(2-propenyl)-	5.3	3.9	2.3	0.0	1.0	5.0
Phenol, 2-methoxy-4-(1-propenyl)-	0.0	0.4	2.6	0.6	0.0	2.7
Catechols						
1,2-Benzenediol	1.0	1.8	1.2	1.3	2.8	1.3
1,2-Benzenediol, 3-methoxy-	2.2	2.7	0.5	0.0	0.0	1.4
1,2-Benzenediol, 4-methyl-	0.4	1.3	1.9	1.5	2.5	1.6
1,2-Benzenediol, 3-methyl-	0.0	1.3	1.1	2.5	2.7	0.3

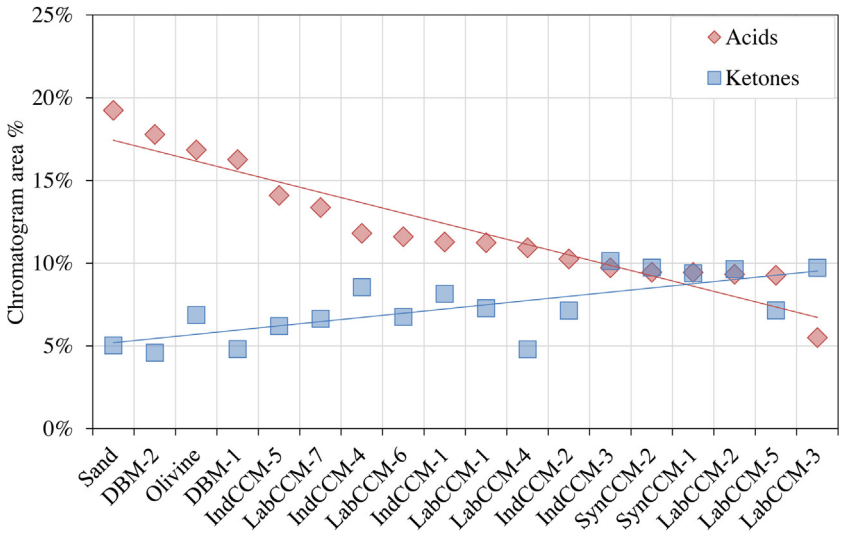

Fig. 10. Correlation between organic acids and ketones in the various MgO and olivine catalytic bio-oils.

in terms of bio-oil deoxygenation *via* the most preferred reaction pathway of CO_2 formation, as discussed above.

It has to be noted, as also pointed out above, that the data presented for ZSM-5 refers to an industrial catalyst formulation comprising of 30 wt.% pure zeolite, the rest being silica-alumina matrix. When a highly acidic, pure ZSM-5 zeolite is used, a substantial decrease of oxygen content can be achieved (ca. 4 wt.% oxygen on organic fraction) accompanied, however, by a dramatic reduction of the organic fraction yield (ca. 5 wt.% on biomass) [35]. Thus, the results presented in this study are more representative of a pilot scale operation [36] where such diluted zeolite formulations are being used and can be directly utilized to evaluate a potential commercial use of the basic natural MgO catalysts.

3.2.4. *Effect of catalyst type on bio-oil composition*

The bio-oil composition obtained from the non-catalytic and catalytic runs, as determined by analysis with the GC–MS system, is presented in Table 6. Bio-oil is a complex mixture of organic, mainly oxygenated, compounds and thus, more than hundred peaks were present in each chromatogram. In order to make the GC–MS analysis results more comprehensible, the identified compounds were categorized in groups, depending on their nature and functionality. These groups were aromatic hydrocarbons (AR; containing only benzene and monocyclic substituted derivatives), aliphatic hydrocarbons (ALI), phenolics (PH), furans (FUR), acids (AC), esters (EST), alcohols (AL), ethers (ETH), aldehydes (ALD), ketones (KET), polycyclic aromatic hydrocarbons (PAH) and nitrogen compounds (NIT). In addition, it should be noted that the GC–MS analysis presented below is semi-quantitative based on percentages of the chromatogram peak areas. This type of analysis serves as an indication of the catalytic effect on bio-oil rather than an accurate quantification of the chemical compounds detected in each case.

As shown in Table 6, the thermal bio-oil is composed mainly of phenolics, acids and ketones. The phenolic compounds in the thermal bio-oil consisted mostly of alkoxy-phenols, catechols and larger molecules with multiple substitutes. Only about 10% was attributed to phenol and alkyl-phenols, as can be seen in Fig. 9, which shows an exponential variation of the relative concentration of these compounds with the organic fraction yield. Other oxygenates were also present, such as ethers and aldehydes, but their total area percentage was relatively small. The most abundant compounds detected in the non-catalytic bio-oil as well as in those derived from selected catalysts are shown in Table 7. The bio-oil produced with the acidic ZSM-5 had significantly reduced acid content compared to the non-catalytic thermal bio-oil (7.4% versus 19.2%, mainly due to conversion of acetic acid, see Table 7) and increased aromatic hydrocarbons (5.1% versus zero), PAH (1.8% versus zero) and phenolics (35.4% versus 28%) content (Table 6). The composition of the phenolic fraction was different than that of the thermal bio-oil; about 25% of the phenolics chromatogram area was attributed to phenol and alkyl-phenols (cresols, xylenols etc.), with the rest being attributed to more oxygenated molecules, such as catechols and alkoxy-phenols (syringol, guaiacol, etc.) (Fig. 9 and Table 7). Overall, the effect of ZSM-5 was the expected one based on the known reaction mechanisms that it catalyzes in biomass fast pyrolysis [11,35,40]. The acid sites of the zeolite facilitated the transformation of the oxygenated compounds (mainly acids) in the pyrolysis vapors towards more desirable compounds, such as aromatic hydrocarbons, while larger fraction of lignin oligomers were converted to light, less-oxygenated phenols, resulting in a bio-oil with improved properties (reduced acidity, increased calorific value and stability, and higher potential for utilization and downstream upgrading).

A similar, slightly lower, decrease in the total chromatogram area of acidic compounds was observed with most of the MgO catalysts, *i.e.* 5.5–14% acids depending on the MgO catalyst, compared to 7.4% and 19.2% for the ZSM-5 and non-catalytic bio-oil respectively (Tables 6 and 7). Contrary to what was observed with the acidic ZSM-5, there was no significant increase of aromatic hydrocarbons or PAH due to the absence of acid sites in the MgO catalysts, which are necessary for the aromatization reactions (Table 6). On the other hand, a significant increase of ketones was observed with most of the MgO catalysts, in contrast to ZSM-5 (Table 6). This was attributed to the basicity of these materials, which catalyzes ketonization reactions that convert the acidic compounds in the pyrolysis vapors to ketones. Ketonization is accompanied by CO_2 formation, which can also explain the increased CO_2 yield that was observed with the MgO catalysts (Table 5). In the case of acetic acid, which is the most abundant acid in bio-oils, as well as in the non-catalytic bio-oil of the present study, the overall ketonization reaction catalyzed by MgO is shown below:

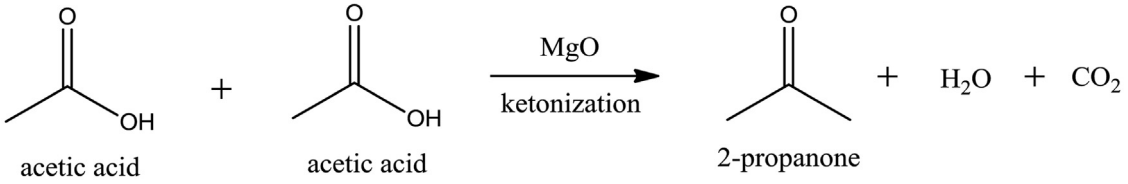

The resulting 2-propanone (acetone) was detected in small amounts in the various catalytic bio-oils, as was readily converted to higher molecular weight ketones, mainly cyclic aliphatic ketones, as can be seen in Table 7. The correlation between ketones and acids in the non-catalytic and the MgO derived bio-oils is presented in Fig. 10. A clear trend is noted, where a decrease in the acids is accompanied by an increase of ketones. Acidic zeolites (*i.e.* ZSM-5), would typically crack molecules such as low MW acids towards even lighter products, *i.e.* CO, CO_2 and light gas hydrocarbons, while also forming aromatic hydrocarbons *via* aromatization of gaseous alkenes (*i.e.* ethylene). On the other hand, MgOs enhance

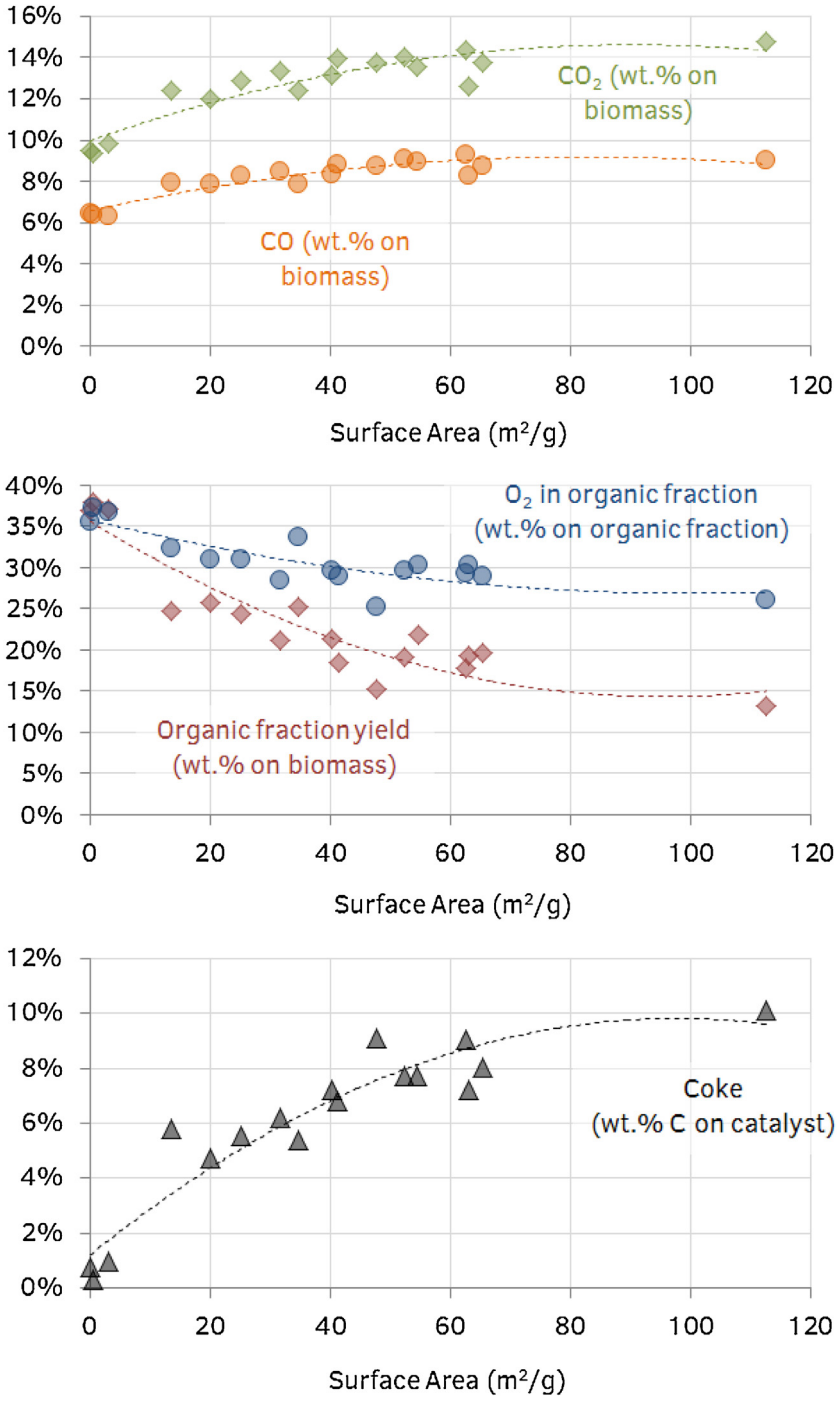

Fig. 11. Effect of MgO catalyst surface area on yields of CO_2 and CO, yield of organic fraction of bio-oil, oxygen content of the organic fraction and coke (catalytic) yield.

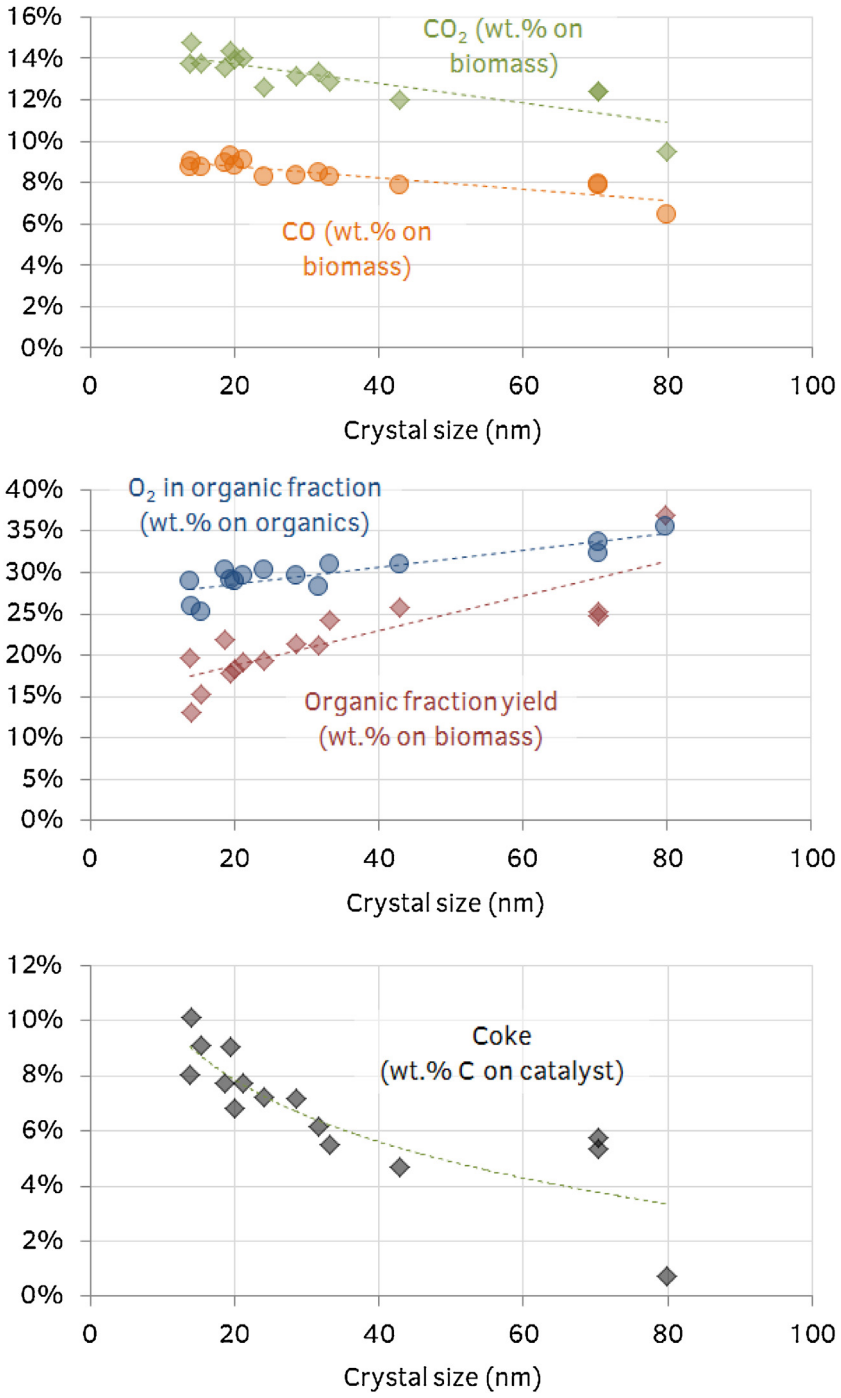

Fig. 12. Effect of crystal size of MgO catalysts on yields of CO_2 and CO, yield of organic fraction of bio-oil, oxygen content of the organic fraction and coke (catalytic) yield.

carbon coupling reactions, forming higher MW products, such as the ketones detected (Table 7). This essentially increases carbon efficiency towards liquid products, which is key to maximizing the overall process efficiency and can lead to alternative concepts of down-stream bio-oil valorization, as discussed below.

The total phenols were also increased with most of the MgO catalysts (Table 6). As with ZSM-5, the percentage of phenol plus alkylated phenols fraction was significantly higher in the MgO catalytic bio-oils compared to the thermal bio-oil (Fig. 9).

3.2.5. Correlation of product yields and bio-oil oxygen content with catalyst physicochemical properties

The effect of critical catalyst physicochemical properties (*i.e.* surface area, crystal size and basicity) on the yields of CO_2, CO, organic fraction of bio-oil, as well as on the oxygen content of the organic fraction is depicted in Figs. 11–13 . The CO_2 and CO gas yields were increased as the catalyst surface area increased (Fig. 11). Accordingly, the organic fraction yield decreased for catalysts with higher surface area, along with the oxygen content of the organic fraction. In addition, coke formation was progressively increased with increasing catalyst surface area (Fig. 11).

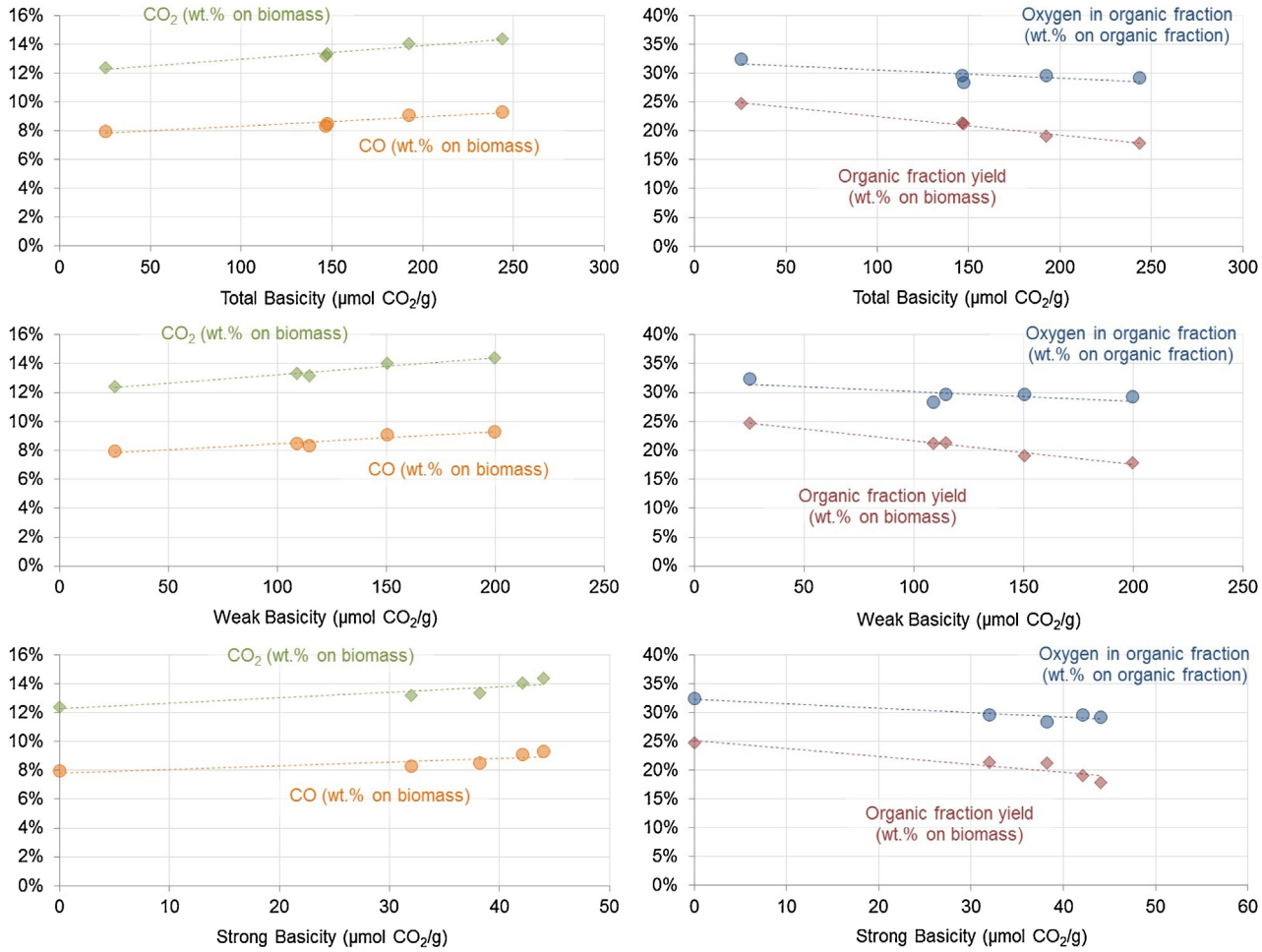

Fig. 13. Effect of total, weak/medium and strong basicity of the high-purity MgO catalysts tested in the present work, on yields of CO_2 and CO, yield of organic fraction of bio-oil and oxygen content of the organic fraction.

In Fig. 12, it can be seen that the smaller crystal size increased the reactivity of the MgO catalysts leading to lower organic fraction yield and oxygen content of the organic fraction, as well as to higher coke production, all obeying to a relatively smooth correlation curve with crystal size. Accordingly, the CO and CO_2 gas yields were increased with decrease of crystal size, as can be seen by the respective correlation curves in Fig. 12. This inversion in the trends of product yields compared to those plotted versus surface area (Fig. 11), is justified by the smooth correlation existing between crystal size and surface area, shown in Fig. 3. Thus, the primary physicochemical characteristics of MgO catalysts, that affect its pyrolysis activity, is the crystal/particle size and morphology, which in turn, affect their porosity and textural properties.

The effect of the total, weak/medium and strong basicity of all the MgO catalysts tested in the present work is depicted in the graphs of Figs. S-1and S-2 (Supporting information). Increased basicity, either weak/medium or strong, induced an increase in the CO and CO_2 gas yields (Fig. S-1). Organic fraction yield and oxygen content seemed also to decrease with higher catalyst basicity, but the data was significantly scattered in these two cases (Fig. S-1). Similarly, the yield of catalytic coke is increased with basicity but with low degree of correlation (Fig. S-2). As discussed in section 3.1.5, the basic properties of the various MgO catalysts depended not only on crystal/particle size and surface area, but also on the presence of impurities (ca. CaO, SiO_2). Thus, when the product yields and oxygen content data were plotted against the basic sites of a separate sub-group of MgO catalysts, *i.e.* that of the high-purity MgOs, the resulting trends exhibited a high degree of correlation, as can be seen in Figs. 13 and 14. To this end, the catalytic data was not well-correlated with the basicity of the low-purity MgOs (Figs. S-3 and S-4). Based on the above data, it can be suggested that the smaller crystal size, the higher surface area and the higher basicity of the natural MgO catalysts, which appear to be interconnected, lead to more reactive biomass fast pyrolysis catalysts, in terms of bio-oil deoxygenation, reduction of organic bio-oil yield and catalytic coke formation.

4. Conclusions

MgO catalysts with various physicochemical characteristics were produced *via* calcination of natural magnesite ($MgCO_3$). The calcination temperature and residence time in the furnace were very important factors, determining the structural, morphological, textural/porous and basicity characteristics of the produced caustic calcined magnesias (CCM) and dead-burnt magnesias (DBM). The increase in temperature and baking time resulted in the formation of larger MgO crystal sizes (*i.e.*, 12–80 nm) and thus to lower specific surface area of ca. 113–0.05 m^2/g since all the MgO materials exhibited solely inter-crystal/particle porosity in the range of mesopores or macropores with average diameters of ca. 10–45 nm. The natural CCM MgOs that have been calcined at conventional industrial conditions (ca. 800–1200 °C) exhibited good thermal stability, in terms of retaining crystal size, surface area and other related properties. The basicity of CCM MgOs was favored by the higher surface

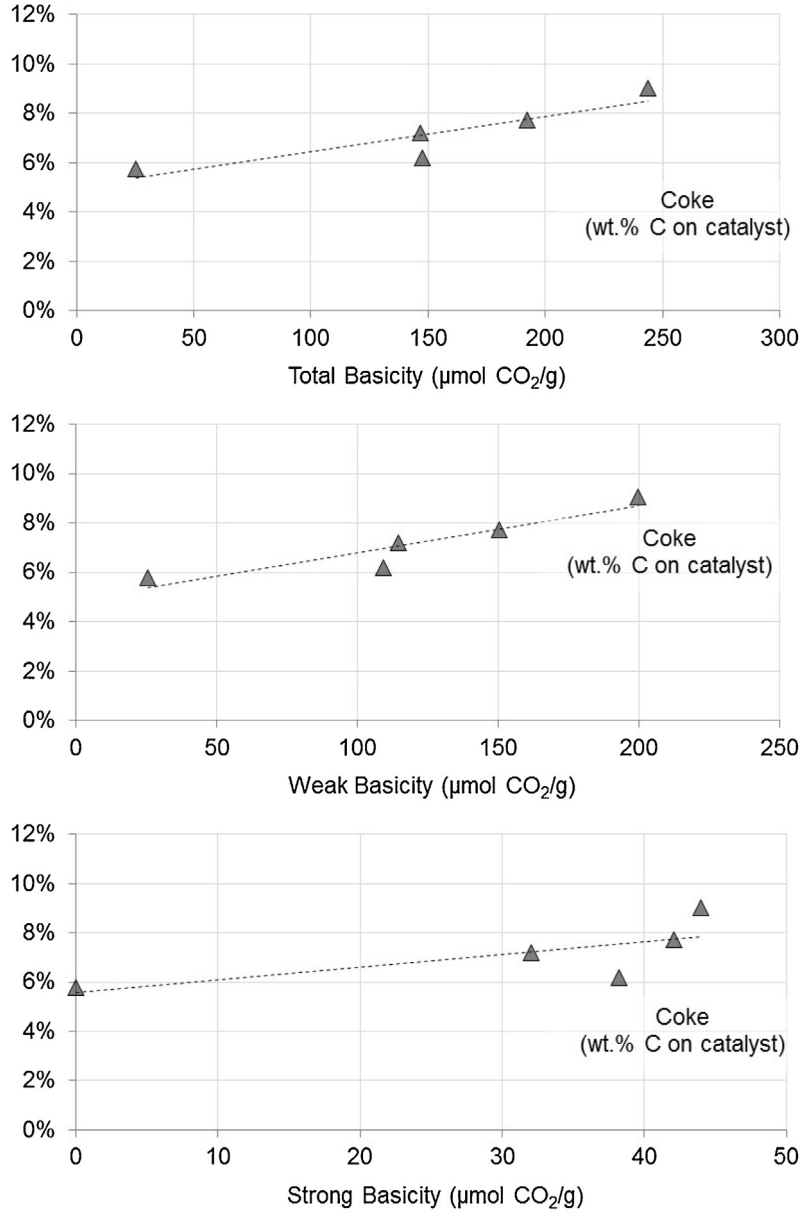

Fig. 14. Effect of total, weak/medium and strong basicity of the high-pyrity MgO catalysts tested in the present work, on catalytic coke formation.

area, mainly by inducing higher number of weak/medium strength basic sites. In addition to surface area, the presence of impurities in the natural CCMs, such as CaO, contributed to the basic sites of higher strength. The MgO catalysts showed negligible acidity, of Lewis type, and irrespective of the amount of impurities.

Despite the lack of acidity, the investigated synthetic and natural CCM catalysts exhibited comparable activity in the catalytic pyrolysis of biomass to that of a diluted, industrial ZSM-5 zeolite catalyst. In general, MgOs with increased mesoporous surface area and/or textural porosity and external surface, exhibited enhanced activity in the conversion of the organic phase of bio-oil, producing less water and more gases and coke when compared to the ZSM-5 catalysts at similar organic fraction yield. The DBM MgOs and olivine catalysts showed very low activity, due to their negligible surface area and poor basic properties. The presence of impurities (*i.e.* oxides of Si, Ca, Fe, etc.) had no clear and identifiable effect on reactivity and product yields.

Based on the product yields and catalyst physicochemical properties, different reaction mechanisms were suggested to prevail compared to those applied for the acidic ZSM-5 zeolite catalysts. The most important pathways identified by the use of MgOs were the carbon coupling reactions, such as ketonization and aldol condensation, both being responsible for the enhanced deoxygenation of bio-oils achieved. When compared to the performance of the ZSM-5 catalyst, the MgO catalysts were able to produce either similar bio-oil organic fraction yield with lower oxygen content or similar oxygen content with higher organics yield. Interestingly, oxygen was removed by the use of MgO catalysts, primarily, *via* the preferred formation of CO_2 instead of CO and/or water. Other important effects on the composition of bio-oil, which affect also its properties, were the significant reduction of acids, the negligible amount of polycyclic aromatic hydrocarbons (PAHs) and the high content of phenolics. A significant difference with the bio-oil produced by ZSM-5 is the absence of the high value (mono)aromatics (BTX), that are being produced by the Brønsted acidity of the zeolitic catalysts.

Acknowledgements

The authors wish to acknowledge co-funding of this research by European Union- European Regional Development Fund and Greek Ministry of Education/GGET, through ESPA 2007–2013/Action "SYNERGASIA-I" (09SYN-42-791).

Appendix A. Supplementary data

Supplementary data associated with this article can be found, in the online version, at http://dx.doi.org/10.1016/j.apcatb.2016.05.031.

References

[1] H.B. Goyal, D. Seal, R.C. Saxena, Renew. Sustain. Energy Rev. 12 (2008) 504–517.
[2] G.W. Huber, S. Iborra, A. Corma, Chem. Rev. 106 (2006) 4044–4098.
[3] J.N. Chheda, G.W. Huber, J.A. Dumesic, Angew. Chem. Int. Ed. 46 (2007) 7164–7183.
[4] L.D. Schmidt, P.J. Dauenhauer, Nature 447 (2007) 914–915.
[5] A.V. Bridgwater, Chem. Eng. J. 91 (2003) 87–102.
[6] D. Carpenter, T.L. Westover, S. Czernik, W. Jablonski, Green Chem. 16 (2014) 384–406.
[7] M. Jahirul, M. Rasul, A. Chowdhury, N. Ashwath, Energies 5 (2012) 4952–5001.
[8] D. Vamvuka, Int. J. Energy Res. 35 (2011) 835–862.
[9] D. Mohan, C.U.J. Pittman, P.H. Steele, Energy Fuel 20 (2006) 848–889.
[10] N. Thegarid, G. Fogassy, Y. Schuurman, C. Mirodatos, S. Stefanidis, E.F. Iliopoulou, K. Kalogiannis, A.A. Lappas, Appl. Catal. B: Environ. 145 (2014) 161–166.
[11] A.A. Lappas, K.G. Kalogiannis, E.F. Iliopoulou, K.S. Triantafyllidis, S.D. Stefanidis, WENE 1 (2012) 285–297.
[12] A. Sanna, J.M. Andrésen, ChemSusChem 5 (2012) 1944–1957.
[13] M. Stocker, Angew. Chem. Int. Ed. 47 (2008) 9200–9211.
[14] S.D. Stefanidis, K.G. Kalogiannis, E.F. Iliopoulou, A.A. Lappas, P.A. Pilavachi, Bioresour. Technol. 102 (2011) 8261–8267.
[15] K.S. Triantafyllidis, E.F. Iliopoulou, E.V. Antonakou, A.A. Lappas, H. Wang, T.J. Pinnavaia, Microporous Mesoporous Mater. 99 (2007) 132–139.
[16] E. Antonakou, A. Lappas, M.H. Nilsen, A. Bouzga, M. Stocker, Fuel 85 (2006) 2202–2212.
[17] T.R. Carlson, T.P. Vispute, G.W. Huber, ChemSusChem 1 (2008) 397–400.
[18] T.R. Carlson, Y.-T. Cheng, J. Jae, G.W. Huber, Energy Environ. Sci. 4 (2011) 145–161.
[19] A. Aho, N. Kumar, K. Eranen, T. Salmi, B. Holmbom, P. Backman, M. Hupa, D.Y. Murzin, Biofuels 1 (2010) 261–273.
[20] K. Wang, K.H. Kim, R.C. Brown, Green Chem. 16 (2014) 727–735.
[21] S. Du, J.A. Valla, G.M. Bollas, Green Chem. 15 (2013) 3214.
[22] J. Jae, G.A. Tompsett, A.J. Foster, K.D. Hammond, S.M. Auerbach, R.F. Lobo, G.W. Huber, J. Catal. 279 (2011) 257–268.
[23] L. Deng, Y. Fu, Q.X. Guo, Energy Fuel 23 (2008) 564–568.
[24] C.A. Gaertner, J.C. Serrano-Ruiz, D.J. Braden, J.A. Dumesic, J. Catal. 266 (2009) 71–78.
[25] B. Li, L. Ou, Q. Dang, P. Meyer, S. Jones, R. Brown, M. Wright, Bioresour. Technol. 196 (2015) 49–56.
[26] G. Li, Z. Li, H. Ma, X. Jiang, W. Yao, Integr. Ferroelectr. 145 (2013) 170–177.
[27] J. Rouquerol, F. Rouquerol, P. Llewellyn, G. Maurin, K.S.W. Sing, Adsorption by Powders and Porous Solids, Academic Press, 2013.
[28] Y.H. Taufiq-Yap, H.V. Lee, M.Z. Hussein, R. Yunus, Biomass Bioenergy 35 (2011) 827–834.
[29] V. García, J.J. Fernández, W. Ruíz, F. Mondragón, A. Moreno, Catal. Commun. 11 (2009) 240–246.
[30] M. Di Serio, M. Ledda, M. Cozzolino, G. Minutillo, R. Tesser, E. Santacesaria, Ind. Eng. Chem. Res. 45 (2006) 3009–3014.
[31] X. Ma, S. Wang, J. Gong, X. Yang, G. Xu, J. Mol. Catal. A: Chem. 222 (2004) 183–187.
[32] S. Kuś, M. Otremba, A. Tórz, M. Taniewski, Appl. Catal. A: Gen. 230 (2002) 263–270.
[33] J.A. Wang, X. Bokhimi, O. Novaro, T. López, R. Gómez, J. Mol. Catal. A: Chem. 145 (1999) 291–300.
[34] S. Stephanidis, C. Nitsos, K. Kalogiannis, E.F. Iliopoulou, A.A. Lappas, K.S. Triantafyllidis, Catal. Today 167 (2011) 37–45.
[35] E.F. Iliopoulou, S.D. Stefanidis, K.G. Kalogiannis, A. Delimitis, A.A. Lappas, K.S. Triantafyllidis, Appl. Catal. B: Environ. 127 (2012) 281–290.
[36] E.F. Iliopoulou, S. Stefanidis, K. Kalogiannis, A.C. Psarras, A. Delimitis, K.S. Triantafyllidis, A.A. Lappas, Green Chem. 16 (2014) 662–674.
[37] M. Guisnet, P. Magnoux, Appl. Catal. A: Gen. 212 (2001) 83–96.
[38] R. Quintana-Solórzano, J.W. Thybaut, G.B. Marin, R. Lødeng, A. Holmen, Catal. Today 107–108 (2005) 619–629.
[39] B. Valle, P. Castaño, M. Olazar, J. Bilbao, A.G. Gayubo, J. Catal. 285 (2012) 304–314.
[40] A.J. Foster, J. Jae, Y.-T. Cheng, G.W. Huber, R.F. Lobo, Appl. Catal. A: Gen. 423–424 (2012) 154–161.